JGR Oceans

RESEARCH ARTICLE
10.1029/2025JC023208

Harbor-Induced Tidal Salinity Dispersion in Partially Stratified Estuaries

D. van Keulen[1,2], **W. M. Kranenburg**[2,3], **and A. J. F. Hoitink**[1]

[1]Department of Environmental Sciences, Hydrology and Quantitative Water Management Group, Wageningen University, Wageningen, The Netherlands, [2]Deltares, Delft, The Netherlands, [3]Department of Hydraulic Engineering, Section Environmental Fluid Mechanics, Delft University of Technology, Delft, The Netherlands

Key Points:

- The instantaneous channel-harbor salt exchange is dominated by a density-driven exchange flow rather than barotropic filling and emptying
- Tidal variations in the exchange flow are controlled by the tidal salinity range in the main channel
- We derive a formula for harbor-induced salt dispersion due to this exchange, revealing the scaling with the salinity range

Correspondence to:
D. van Keulen,
daan.vankeulen@wur.nl

Citation:
van Keulen, D., Kranenburg, W. M., & Hoitink, A. J. F. (2026). Harbor-induced tidal salinity dispersion in partially stratified estuaries. *Journal of Geophysical Research: Oceans*, *131*, e2025JC023208. https://doi.org/10.1029/2025JC023208

Received 25 JUL 2025
Accepted 4 MAR 2026

Author Contributions:
Conceptualization: D. van Keulen
Formal analysis: D. van Keulen
Funding acquisition: A. J. F. Hoitink
Investigation: D. van Keulen
Methodology: D. van Keulen
Supervision: W. M. Kranenburg, A. J. F. Hoitink
Visualization: D. van Keulen
Writing – original draft: D. van Keulen
Writing – review & editing: W. M. Kranenburg, A. J. F. Hoitink

Abstract The contribution of tidal trapping to salt dispersion has been well described for well-mixed estuaries, in terms of barotropic filling and emptying of the traps. How traps contribute to salt dispersion in deeper, partially stratified systems remains underexplored. We investigate the dispersive effect of temporary storage of saltwater in harbors adjacent to a partially stratified estuary using field observations and numerical modeling. Our results show that instantaneous channel–harbor salt exchange is dominated by density-driven exchange flows arising from baroclinic pressure gradients between the channel and the harbors. This pressure gradient, and consequently the exchange flow, reverses during the tide due to tidal variations in main-channel salinity. Quantification of the trapping-induced additional salt transport from individual basins reveals substantial differences in contributions of individual basins. These differences are linked to a region in the main channel where the tidal salinity range has a minimum, thus limiting the set-up of baroclinic pressure gradients, reducing exchange flow strength and tidal trapping. Analysis of the density-driven exchange reveals that it scales with the tidal salinity range raised to the power 3/2. Using this relationship, we derive an expression for the dispersion coefficient associated with density-driven tidal trapping. This formulation indicates that the resulting dispersion is governed by the main-channel tidal excursion length and the propagation speed of the density current within the trap, and that the dispersion coefficient scales with the square root of the along-channel salinity gradient, in contrast to tidal trapping driven by basin filling and emptying, which is independent of this gradient.

Plain Language Summary This study examines how harbor basins contribute to the spreading (or dispersion) of salt in estuaries. Salt exchange between channels and adjacent harbors can occur either due to the filling and emptying of the basins during the tide or due to circulation driven by differences in salinity between the channel and the harbor. Our field observations and numerical modeling results show that the second mechanism quickly dominates, and that the amount of salt exchanged during the tide strongly depends on the variation of salinity in the main channel over the tidal cycle. The temporary storage and release of salt in the harbor contributes to the redistribution and spreading of salt along the estuary. We derived an expression for salt dispersion due to the second exchange mechanism, which shows how the total spreading effect depends on the salt variation in the main channel over the tide. This dependence differs from existing expressions derived for the first exchange mechanism.

1. Introduction

The intrusion of salt in estuaries is governed by a continuous interplay between freshwater flushing from river discharge and dispersive mechanisms that drive an up-estuary salt transport. The importance of different dispersive transport mechanisms differs between systems (Dijkstra & Schuttelaars, 2021). When the salinity intrusion length is much longer than the tidal excursion, the salt balance is often controlled by the estuarine circulation resulting from the gravitational circulation (Chatwin, 1976; Hansen & Rattray, 1965) and tidal straining (Simpson et al., 1990). When both length scales are of similar magnitude, as in short estuaries, tidal dispersion becomes the principal mechanism of landward salt transport (Fischer et al., 1979; W. R. Geyer & Signell, 1992). Nevertheless, even when estuarine circulation dominates at the system scale, tidal dispersive processes can remain locally important, particularly in the upper estuary where tidal dispersion often becomes the dominant transport mechanism (Dijkstra et al., 2022).

Geometric features, such as intertidal areas, creeks, harbors, and other channel irregularities creating dead zones adjacent to the main channel, can temporarily store volumes of saltwater within the tidal cycle and release them

later. When the release occurs at a different position along the tidal excursion than where it originally comes from, a net redistribution of salt occurs over a distance equal to the tidal excursion length within a single tidal cycle (Dronkers, 1978). However, the effect of this redistribution depends on the along-channel salinity structure and therefore may either enhance or reduce the net salt transport in the main channel associated with tidal dispersion. The overall impact of these geometric features is often system-dependent (Hendrickx & Pearson, 2024). For example, in well-mixed estuaries, intertidal areas tend to enhance salinity intrusion by increasing tidal dispersion, whereas, in partially mixed or stratified systems, the increase in the tidal prisms and tidal currents due to these features are likely to reduce the estuarine circulation, which is the dominant transport mechanism in such environments. In this study, we investigate the exchange between channels and harbors and the associated contribution to salinity dispersion in partially stratified estuarine systems.

Salt transport decomposition techniques (Fischer et al., 1979; Lerczak et al., 2006) can be used to mathematically decompose the total salt transport through a cross-section and quantify the individual contributions associated with different salt transport mechanisms, based on observations or model results. Within such decompositions, tidal dispersion manifests itself in the temporal correlation between the cross-sectionally averaged tidally varying velocity and salinity signals (Dronkers & Van de Kreeke, 1986; Fischer et al., 1979). However, such a transport decomposition provides limited insight into the underlying mechanisms, as the observed correlation results from exchange processes occurring elsewhere. The work by Dronkers and Van de Kreeke (1986) showed that the salt transport associated with this temporal correlation, when determined in an Eulerian reference frame, arises from shear occurring elsewhere within the tidal excursion domain and is therefore termed non-local salt transport. The Lagrangian approach of Dronkers and Van de Kreeke (1986) can be used to study the origin of the tidal salt transport through a cross-section, as was demonstrated by Garcia and Geyer (2022). An alternative approach, which focuses more directly on isolating the influence of individual geometric features and parameterizing their dispersive contribution, was proposed by Dronkers (1978) and extended by Van Keulen et al. (2025). This methodology quantifies the net salt transport into or out of a storage region (often called traps) over a tidal excursion, thereby directly assessing the redistribution effect of a single feature. Whereas the approach of Dronkers and Van de Kreeke (1986) provides insight into the overall resulting salt transport, the advantage of the approach of Dronkers (1978) is that it enables assessment of the relative importance of different channel–trap exchange mechanisms (Van Keulen et al., 2025). This is the approach adopted in the present study.

The temporal storage in a trap can result from two types of exchange mechanisms. The first mechanism is referred to as advective out-of-phase exchange, in which a trap is filling and emptying by the barotropic tide. When there is a velocity phase difference between the main channel and a trap, the trapped volumes will reenter the channel at a different location than where they left it, relative to the oscillating water mass in the main channel. Consequently, trapped and non-trapped parcels experience, respectively, a net down- and up-estuary displacement relative to each other (Dronkers, 1978; Van Keulen et al., 2025). The resulting salinity dispersion is largest for the maximum physically realistic velocity phase difference of 90° between the channel and a trap. Mixing of the salinity field trapped during the barotropic flood can enhance the dispersive effect when the phase difference between velocity variation in the trap and in the main channel is small (Dronkers, 1978; Van Keulen et al., 2025). This mechanism was also visible in the observations of Garcia et al. (2022), who showed that the trapped salinity field was (partially) mixed by a baroclinic circulation within the trap, causing relatively low-salinity water to leave the trap earlier during the onset of the barotropic ebb flow in the trap.

The second mechanism occurs when the exchange of salt between the channel and the trap across the trap entrance is diffusive in nature (Dronkers, 1978; Okubo, 1973), driven by density-driven exchange or turbulent processes. Okubo (1973) derived an elegant formulation for the dispersive effect of a continuous lateral trap undergoing diffusive exchange with the main channel. However, his formulation relies on a constant exchange rate coefficient that reflects the strength of the exchange, but does not describe a specific mechanism. Okubo (1973) noted this and suggested this to be a direction for future refinement. Both observational and modeling studies have explored the diffusive exchange processes between the channel and the trap (Garcia et al., 2022; Ralston & Stacey, 2005), but have not proceeded to describe them in more precise formulations of the exchange and the resulting dispersion. Van Keulen et al. (2025) explored the combined effect of both advective out-of-phase exchange and diffusive exchange driving the transport of salt across the trap entrance. They show how this combined effect depends on a Péclet number for tidal trapping. In addition, their results indicated that the resulting additional up-estuary salt transport does not necessarily increase when the diffusive exchange becomes stronger, especially for larger velocity phase differences.

The specific processes of channel–harbor exchange have been studied by for example, Roelfzema and Van Os (1978), Abraham et al. (1986), Eysink (1989), De Nijs et al. (2009), and van Maren et al. (2009). These studies show that the exchange of salt results from tidal filling and emptying, eddies, and density-driven exchange. The density-driven exchange is established by the advection of the salinity field in the main channel, generating a channel–harbor density difference that drives a lock-exchange type flow. This flow reverses direction within the tidal cycle (Abraham et al., 1986; De Nijs et al., 2009; van Maren et al., 2009). The characteristics of this type of exchange are influenced by the phasing and properties of the salinity field in the main channel and, on longer timescales, by hydrodynamic conditions such as storm surges (De Nijs et al., 2009). Moreover, van Maren et al. (2009) found that dock length influences the phasing and strength of the exchange flow, depending on the size of the harbor basins relative to the forcing conditions. The work of both De Nijs et al. (2009) and van Maren et al. (2009) focused on harbor siltation rather than salt dispersion. Early work by Roelfzema and Van Os (1978) and Abraham et al. (1986) investigated the influence of harbors on the salt intrusion length. Their results show that salt intrusion may increase due to the temporal storage and release of salt in a harbor. More specifically, Roelfzema and Van Os (1978) observed a relation between the strength of density-driven channel–harbor exchange and the salt intrusion length, but they did not quantify the actual dispersive effect of tidal trapping.

In this paper, we investigate the exchange of salt between a channel and an adjacent harbor, quantify the additional up-estuary salt transport generated by tidal trapping, and provide insights into the mechanisms by which tidal trapping governs salt dispersion in deeper, partially stratified systems. We do this based on field observations and numerical modeling of the channel-harbor salt exchange in the New Meuse, a branch of the Rhine-Meuse Estuary. The structure of this paper is as follows. Section 2 describes the field site, the set-up of the field measurements, the hydrodynamic model and the analysis approach. Section 3 presents the field observations, revealing marked differences in channel–harbor exchange for the two harbors surveyed during the 13-hr shipboard campaigns. Section 4 presents numerical model results that verify the different processes observed during the shipboard measurements and provide an explanation for the observations. Subsequently, we evaluate the additional up-estuary salt transport resulting from channel-trap exchange (i.e., tidal trapping induced dispersion) for different harbors using the modeled channel-harbor exchange. In Section 5, we evaluate the role of tidal trapping in partially stratified systems and compare this with the classical understanding of tidal trapping in well-mixed systems. Within this comparison, we introduce a new formulation for the dispersion coefficient associated with density-driven tidal trapping. Conclusions are drawn in Section 6.

2. Methods

2.1. Study Area

The NM and the New Waterway are part of the Rhine–Meuse Estuary (Figures 1a–1c). The Rhine-Meuse Estuary consists of a southern branch, composed of the Haringvliet (HV) and Hollands Diep, and the northern branch, which includes the New Waterway (NWW) and the NM. The southern branch is a former estuary where discharge is regulated through sluices at the mouth. The northern and southern branches are interconnected through several smaller channels, forming a complex channel network (Figure 1b). The New Waterway and NM channels serve as major shipping routes and host several harbors along the main channel, which are investigated in this study. The locations of the larger harbors studied here are shown in Figure 1c.

Freshwater input into the Rhine-Meuse estuary is supplied by the Waal, Lek, and Maas rivers, which on average contribute 70%, 16%, and 14% of the total discharge, respectively (Leuven et al., 2023). Since the Waal and Lek are both bifurcations of the Rhine, freshwater forcing is typically expressed through the Rhine discharge measured at Lobith (Figure 1a). Under average discharge conditions, approximately 14% of the freshwater is transported to the North Sea through the southern estuary, while the remaining 86% exits the channel network via the northern branch (Cox et al., 2021). Because the southern branch is closed off by sluices, nearly all tidal energy enters the system through the northern branch.

2.2. Moored and Shipboard Measurements

A monitoring campaign was conducted in the NM from 01-06-2022 to 24-10-2022. Two bottom-moored upward-looking ADCPs (600 kHz, manufactured by Teledyne RDI) were deployed in the NM (Figure 1c), and two CTD arrays, each equipped with two CTD sensors, were attached to the nearby navigation buoys. A third array was installed further up-estuary. Maintenance on the CTD probes was performed every 3–4 weeks to limit the effects

10.1029/2025JC023208

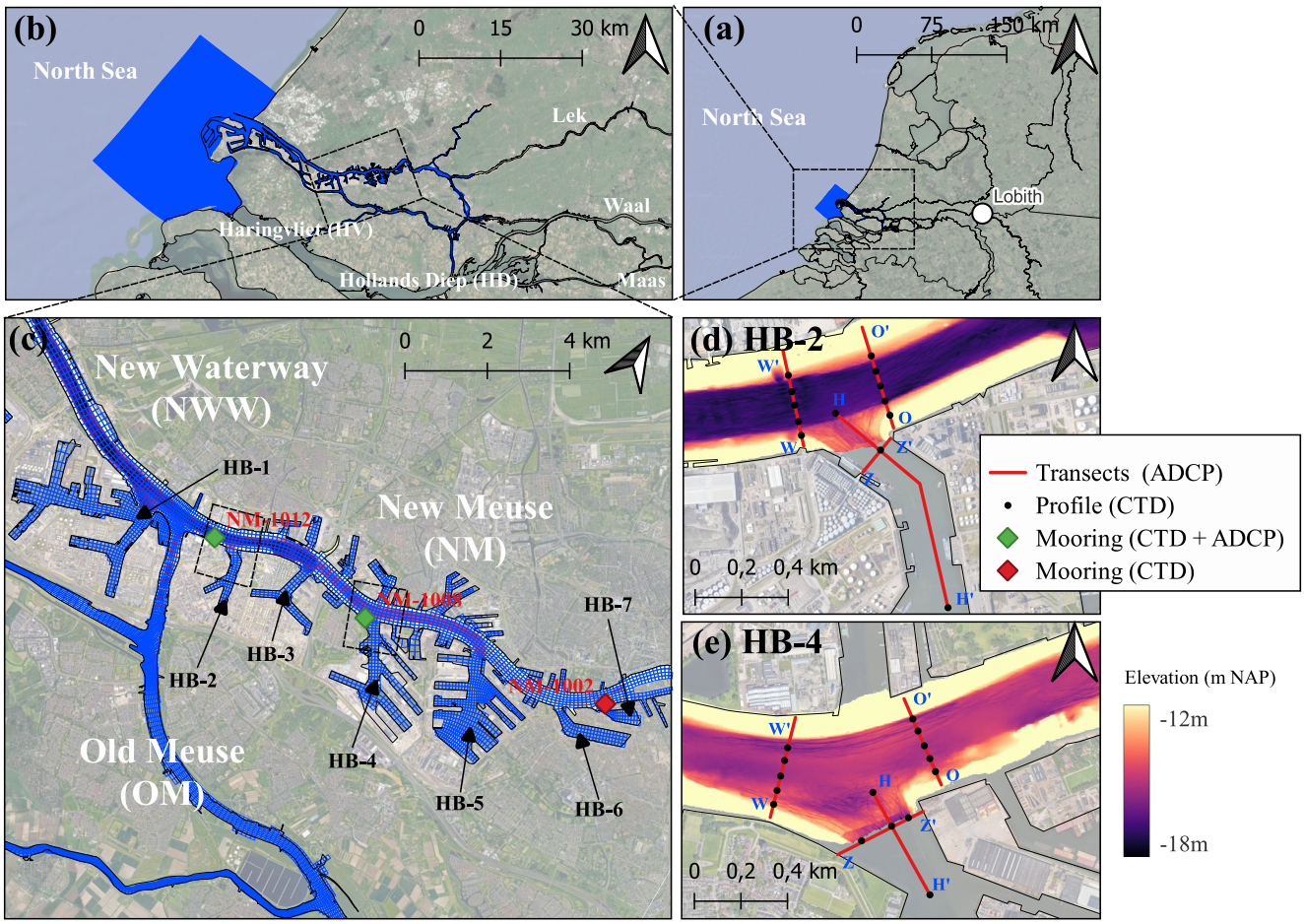

Figure 1. Satellite images of the Rhine–Meuse Delta, the model domain, and main branches. (a) Location of the Rhine–Meuse Estuary in the Netherlands. (b) Zoom of the lower Rhine–Meuse Estuary and extent of the model domain (dark blue colors indicate the numerical grid). (c) Overview of the New Meuse showing the studied harbors and moored measurement sites. (d) Setup of the 13-hr shipboard survey at site HB-2. (e) Setup of the 13-hr shipboard survey at site HB-4.

of biofouling. The locations of these CTD moorings are shown in Figure 1c. A water level gauge maintained by Rijkswaterstaat is located just upstream of NM-1012. The mooring data is used here to examine the along-channel salinity distribution in the NM during the monitoring period.

A total of four 13-hr shipboard measurement campaigns were conducted at sites HB-4 and HB-2 under neap- and spring-tide conditions (Figures 1d and 1e). The data obtained is primarily used here to investigate the exchange of salt between the channel and the harbor. From a research vessel, ADCP measurements and vertical CTD profiles were collected along the transects shown in Figures 1d and 1e, providing additional insight into the flow and salinity structure. At HB-4, completing one full cycle consisting of ADCP transects and CTD profiles at all cross-sections took 60–70 min, while at HB-2 it took 45–55 min. The ADCP data were processed using ADCPTOOLS (Vermeulen et al., 2014), applying the regularization method developed by Jongbloed et al. (2025). The processed shipboard ADCP data were projected onto a mesh with a vertical resolution of $\Delta z = 0.5$ m and a grid size of $\Delta y = 10$ m.

2.3. Numerical Hydrodynamic Modeling

The 13-hr shipboard measurements provide insight into channel–harbor exchange. However, direct comparison of the non-synchronous records across locations is challenging due to the daily inequality of the tide, fluctuating river discharge, and surge-induced variations, which all contribute to unsteadiness in the salinity field. Estimating the trapping effect (see Section 2.4.3) and computing tidally averaged salt fluxes from the data is challenging because of the limited time span of the 13-hr measurements.

Table 1
Overview of Rhine River Discharge Q^{riv} Statistics (Mean, 10th and 90th Percentiles) Measured at Lobith, Along With Surge Variations (Standard Deviation, 5th and 95th Percentiles) From a Nearby Tide Gauge

Data set	Mean(Q^{riv}) ($m^3\ s^{-1}$)	Q^{riv}(10%) ($m^3\ s^{-1}$)	Q^{riv}(90%) ($m^3\ s^{-1}$)	Std(η^{surge}) (m)	η^{surge}(5%) (m)	η^{surge}(95%) (m)
Reference (2010–2020)	2,084	1,118	3,258	0.13	−0.18	0.22
Modeled period (25-09 to 21-10-2015)	1,116	1,034	1,254	0.09	−0.17	0.13
Measurement period (01–09 to 24-10-2022)	1,272	887	1,825	0.16	−0.24	0.33

Note. The surge variations, η^{surge}, represent water level fluctuations in the 25-hr to 14-day frequency band. The table includes data for the modeled period (25-09-2015 to 21-10-2015), a portion of the measurement campaign (01-09-2022 to 24-10-2022, shown in Figure 4), and a reference period 2010–2020.

To support the interpretation of the observations and quantify the effect of tidal trapping, a numerical hydrodynamic model of the Rhine-Meuse Estuary is used (Leuven et al., 2023). The Delft3D model solves the incompressible shallow water equations, with the eddy viscosity and diffusivity modeled using a $k-\epsilon$ scheme (Deltares, 2021). The model domain covers the central and northern branches of the Rine-Meuse Estuary, as well a part of the North Sea (Leuven et al., 2023). The resolution of the computational grid varies, with the coarsest resolution applied to the offshore domain. In the region of interest, cell sizes are approximately 140×80 m. In the vertical, the model uses 20 equidistant σ-layers. Boundary conditions are derived from an overlapping, larger 2D hydrodynamic model.

We used model simulations from Leuven et al. (2023) covering the period 25-09-2015 to 21-10-2015. Although this period does not overlap with our measurement campaign, it was chosen because the model has been well validated for this time frame (Leuven et al., 2023). Discharge at Lobith (Q^{riv}) during this period was low, and comparable to the 10th percentile discharge of the measurement period ($Q^{riv} \approx 1100\ m^3\ s^{-1}$), see Table 1. Moreover, discharge remained relatively constant, and storm surge induced water level variations (η^{surge}) were relatively weak. Here, η^{surge} is defined as the water level variation occurring within the 25-hr to 14-day frequency band. The combination of relatively steady discharge and relative weak surge-induced variations results in relatively stable salinity fields throughout the modeled period. In comparison, the average discharge during our measurement campaign was slightly higher ($Q^{riv} \approx 1300\ m^3\ s^{-1}$, Table 1) largely due to an increase in Rhine

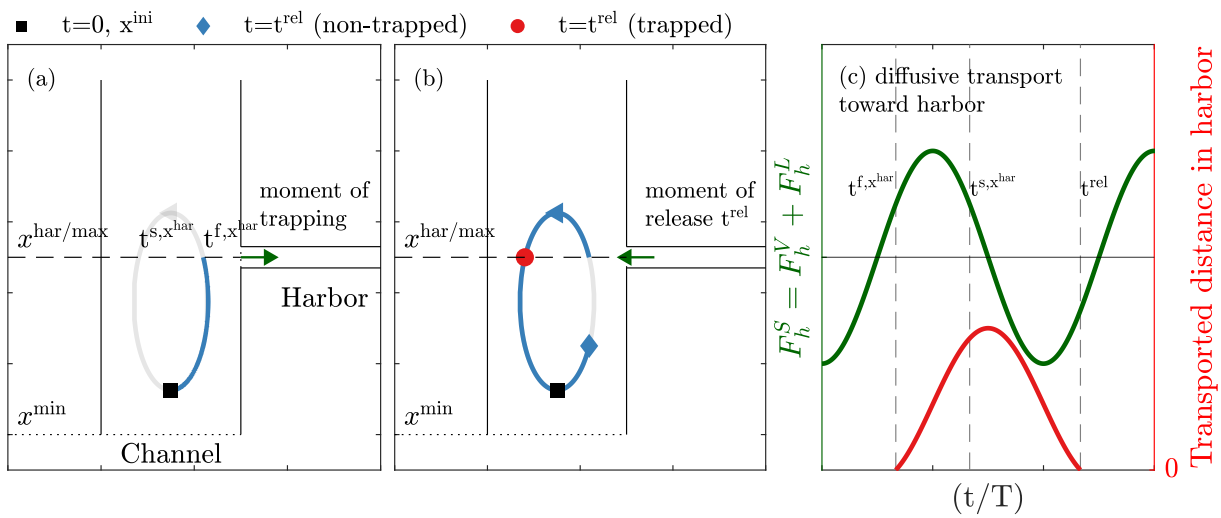

Figure 2. Schematic illustration and notation of tidal trapping through exchange that is diffusive in nature. The reference time (t = 0) corresponds to low-water slack in the main channel and is used to visualize trajectories originating from x^{ini}. Note that the semi-minor axes of the depicted trajectories are shown for illustrative purposes only. (a) Trajectory of a parcel from its initial position at x^{ini} to the trap location x^{har} at time $t^{f,x^{har}}$. During this passage, exchange occurs and a fraction of the parcel is transported into the trap; its displacement is illustrated in panel (c). (b) Continuation of the trajectory of the non-trapped fraction, which passes the trap a second time at $t^{s,x^{har}}$ and continues until the trapped volume is released back into the main channel at time t^{rel}, illustrating the dispersive effect. (c) Illustration of the assumed diffusive exchange between the channel and the harbor, together with the distance traveled by a trapped parcel within the trap.

discharge during the second half of the campaign toward average discharge conditions (see also Figure 4). In addition, surge-induced water level variations were more pronounced during the measurements.

The first 2 weeks were used to spin-up the model and are excluded from the analysis. The model simulation was initialized from a spin-up run, starting from a state in which salinity was close to equilibrium. Model output is stored at cross-sections in the main channel at 1 km intervals and at the entrances of the studied harbors, with a sampling frequency of 10 min.

2.4. Analysis

2.4.1. Salt Transport Decomposition Methods

The instantaneous exchange of salt between the main channel and adjacent harbors is analyzed by decomposing both measured (13-hr shipboard measurements) and modeled fluxes. The decomposed instantaneous salt transport contributions are used to quantify the contribution of different exchange mechanisms (see Section 3.5 and 4.3) and the modeled channel-harbor exchange is used to assess the contribution of tidal trapping to salinity dispersion (see Section 2.4.3).

2.4.2. Instantaneous Salt Transport Decomposition

To decompose the instantaneous salt transport, we follow the approach of Ralston and Stacey (2005), adapted to sigma-layer coordinates. We introduce a non-dimensional lateral coordinate $\gamma = y/B$, where B is the cross-sectional width. The velocity u and salinity s are decomposed as

$$\begin{aligned} s(t,\gamma,\sigma) &= s^A(t) + s^V(t,\sigma) + s^L(t,\gamma,\sigma), \\ u(t,\gamma,\sigma) &= u^A(t) + u^V(t,\sigma) + u^L(t,\gamma,\sigma), \end{aligned} \tag{1}$$

where the superscripts A, V, and L denote the cross-sectional mean, vertical deviation, and lateral residual, respectively. The cross-sectional means are defined as area-weighted averages. The vertical deviation of the velocity is defined as

$$u^V(t,\sigma) = \frac{\int_0^1 \left[u(t,\gamma,\sigma) - u^A(t)\right] h(\gamma,\sigma,t)\, B\, d\gamma}{\int_0^1 h(\gamma,\sigma,t)\, B\, d\gamma}, \tag{2}$$

where $h(\gamma,\sigma,t)$ is the physical thickness of the sigma layer at location γ and normalized vertical coordinate σ. The lateral residual is

$$u^L(t,\gamma,\sigma) = u(t,\gamma,\sigma) - u^A(t) - u^V(t,\sigma), \tag{3}$$

and the salinity field is decomposed analogously. Because sigma layers are terrain-following, the vertical and lateral components of the decomposition are not strictly orthogonal in physical coordinates. However, as the evaluated cross-sections are nearly rectangular, this non-orthogonality is weak and does not significantly influence the relative contributions of the vertical and lateral components to the total salt transport.

The instantaneous salt transport is then decomposed into three contributions:

$$\begin{aligned} F^T(t) &= F^A(t) + F^V(t) + F^L(t) \\ &= u^A(t)\, s^A(t)\, A + \int_0^1 \int_0^1 u^V(t,\sigma)\, s^V(t,\sigma)\, h(\gamma,\sigma,t)\, B\, d\gamma\, d\sigma \\ &\quad + \int_0^1 \int_0^1 u^L(t,\gamma,\sigma)\, s^L(t,\gamma,\sigma)\, h(\gamma,\sigma,t)\, B\, d\gamma\, d\sigma, \end{aligned} \tag{4}$$

where $A = \int_0^1 \int_0^1 h(\gamma,\sigma,t)\, B\, d\gamma\, d\sigma$ is the total cross-sectional area. Equation 4 decomposes the total instantaneous salt transport F_T into three contributions: the cross-sectional average transport F^A, and the transport

associated with the vertical $\left(F^V\right)$ and lateral $\left(F^L\right)$ structures, respectively. To quantify tidal trapping and the contribution of alternative mechanisms, F^A represents the transport associated with advective transport (i.e., tidal filling and emptying), while F^V and F^L represent salt fluxes that, in a cross-sectionally averaged sense, act diffusively and, in the case of channel-harbor exchange, are largely associated with density-driven exchange and horizontal eddies, respectively, among other contributing processes.

Accurate quantification of the cross-sectionally averaged current at the harbor entrance u_h^A from the 13-hr boat surveys at cross-section Z-Z′ proved difficult, because the magnitude of u_h^A (1–10 cm/s) was much smaller than the vertical and lateral variations. Obtaining reliable estimates was further complicated by navigation activities and industrial discharges at HB-2. The cross-sectionally averaged velocity u_h^A is therefore estimated from water level variations, $\frac{d\eta}{dt}$, under the assumption that the harbors behave as short basins (Friedrichs, 2010). In this approach, u_h^A is represented as $u_h^A = \alpha_1 + \alpha_2 \frac{d\eta}{dt}$, with the coefficients α_1 and α_2 determined by linear regression of the observations. We cross-referenced the obtained coefficient with those obtained when performing it on the numerical model, yielding differences between 15% and 30%.

In addition to decomposing the instantaneous salt transport between the channel and harbor, the subtidal salt transport in the main channel are also decomposed to provide insight into the transport mechanisms controlling up-estuary salt transport. For the decomposition of the subtidal transport, a slightly different approach is used, as shown in Appendix A1. The key difference between the decomposition in Appendix A1 and Equation 4 is that no distinction is made between vertical and lateral variations in the cross-section. Instead, the along channel current and salinity field are decomposed into tidally averaged components, deviations from the tidally averaged and similarly into cross-sectionally averaged values and cross-sectional varying components.

2.4.3. Methods to Estimate the Up-Estuary Salt Transport From Tidal Trapping

To quantify the additional up-estuary salt transport resulting from channel–harbor exchange, here we adopt a salt transport balance based on Lagrangian reasoning. This balance (Equation 5) was introduced by Dronkers (1978) and further analyzed by Van Keulen et al. (2025). Using this balance, we assess the tidal trapping from the modeled salt transport.

To illustrate this balance, we consider a trap whose entrance width Δx is much smaller than the tidal excursion length L_c (i.e., $\Delta x \ll L_c$), such that the trap can be treated as a point source–sink. We first consider a deep main channel connected to a dead-end side channel in which the water is effectively stagnant (i.e., $\eta_h/H_h \ll 1$), and exchange between the main channel and the trap is primarily diffusive in nature. In this example, we assume that this diffusive salt transport into the trap is primarily driven by a density current that is 90° out of phase with the main-channel current (illustrated in Figure 2). We then introduce a control plane that moves with the flow in the main channel, starting from its initial position x^{ini} (also Figure 2). This plane passes the trap location at x^{har} twice during a tidal cycle. During the interval between the first $(t^{\mathrm{f},x^{\mathrm{har}}})$ and second $(t^{\mathrm{s},x^{\mathrm{har}}})$ passages, a net transport of salt into the trap occurs. The salt is therefore temporarily stored and, if the tidally averaged transport from the trap over a full cycle is zero, it must subsequently be released upstream of the control plane. Consequently, the volume that is temporarily trapped and released upstream of the control plane must have passed through the cross-section at x^{ini} where the control plane returns to $x^{\mathrm{ini}} = x^{\mathrm{har}}$ after one full cycle. Under quasi-steady-state conditions, the net salt transport through a plane originating at the trap location $\left(x^{\mathrm{ini}} = x^{\mathrm{har}}\right)$ is therefore zero. If the system is not in periodic equilibrium, this net transport represents the tidally averaged salt flux from the trap into the main channel. The above described exchange mechanisms can also be visualized by tracking the displacement of trapped particles relative to non-trapped particles, illustrated in Figure 2. Panel (a) shows the trajectory from its initial position x^{ini} at slack water in the channel to the point where it crosses the trap $(t^{\mathrm{f},x^{\mathrm{har}}})$. During passage past the trap, exchange occurs and a portion of the volume becomes trapped. The non-trapped fraction continues to travel with the main-channel current and passes the trap again after tidal reversal (at time $t^{\mathrm{f},x^{\mathrm{har}}}$). The exchanged volume, however, continues to be transported within the trap by diffusive processes, as the assumed exchange flow is out of phase with the main-channel current (see panel c). At the moment the trapped parcel returns to the main channel, it is located upstream of the non-trapped parcel (see panel b).

In the previous example, the structure of the velocity field is such that a particle traveling with the local current in the main channel returns to its initial location after a full tidal cycle (neglecting Stokes drift and a uniform along

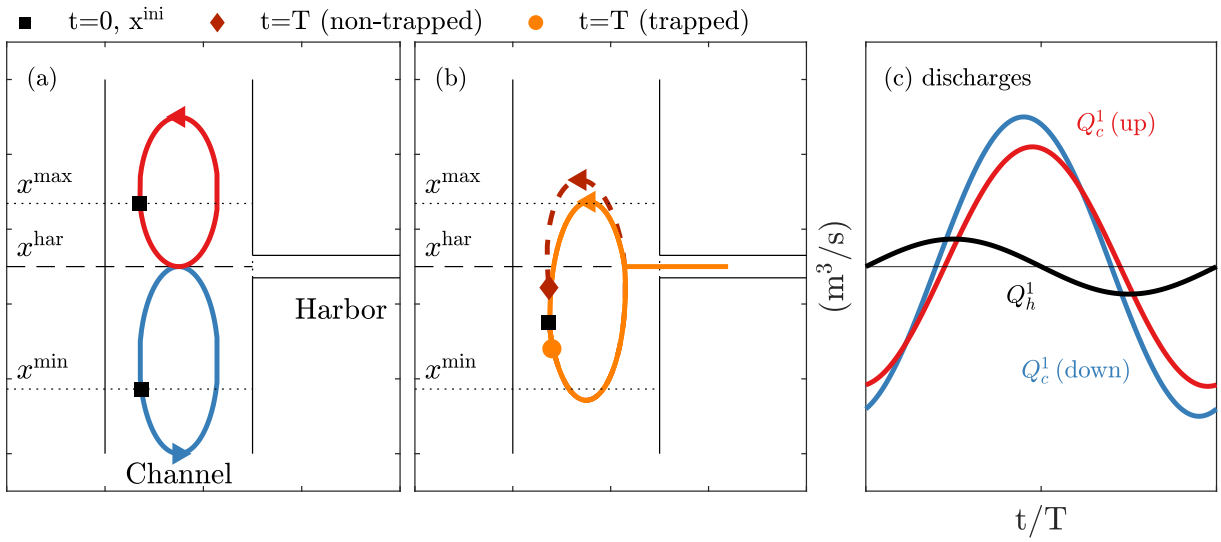

Figure 3. Schematic illustration and notation of tidal trapping through advective out-of-phase exchange. The reference time (t = 0) corresponds to low-water slack in the harbor and is used to visualize trajectories originating from x^{ini}. Note that the semi-minor axes of the depicted trajectories are shown for illustrative purposes only. (a) Trajectories of two water parcels that reach the harbor location at either high- or low-water slack but do not become trapped, illustrating the bounds x^{min} and x^{max}. (d) Trajectories of two water parcels initially located between x^{min} and x^{max}, where one parcel becomes trapped while the other does not, resulting in a net relative displacement from their initial positions. (e) The assumed tidally varying discharge components in the main channel down-estuary of the harbor, Q_c^1 (down), up-estuary of the harbor, Q_c^1 (up), and in the trap, Q_h^1, which introduce the relative motion between the channel and the harbor.

channel current for simplicity). However, the presence of the trap, in which the current is out of phase with the main channel, induces a small phase difference across the length of the trap (see panel a and c in Figure 3). Due to the phase differences between the currents in the main channel and that in trap, the volume that becomes trapped experiences a net relative displacement in the down-estuary direction (panel b). This displacement is compensated by a net up-estuary excursion of the water volume that remains in the main channel, resulting from the phase difference within the main channel over the trap (Dronkers, 1978; Van Keulen et al., 2025). The salt transport through the cross-section at x^{ini} therefore represents the balance between (a) the net salt transport from the trap associated with filling and emptying, and (b) the salt transport resulting from the net up-estuary excursion of the main-channel water volume.

The additional salt transport arising from the above-described process of channel–harbor exchange, $\Delta\tilde{F}_c^{\mathrm{trp}}\left(x^{\mathrm{ini}}\right)$, through the cross-section at x^{ini} in the main channel, is approximated as (Dronkers, 1978; Van Keulen et al., 2025):

$$\Delta\tilde{F}_c^{\mathrm{trp}}\left(x^{\mathrm{ini}}\right)=\begin{cases}\underbrace{\int_{t^{f,x^{\mathrm{har}}}}^{t^{s,x^{\mathrm{har}}}}F_h^V\,dt}_{\tilde{F}_c^V}+\underbrace{\int_{t^{f,x^{\mathrm{har}}}}^{t^{s,x^{\mathrm{har}}}}F_h^L\,dt}_{\tilde{F}_c^L}+\underbrace{\int_{t^{f,x^{\mathrm{har}}}}^{t^{s,x^{\mathrm{har}}}}F_h^A\,dt}_{\tilde{F}_c^A}+\underbrace{\int_{-\delta}^{0}s_c\left(x^{\mathrm{ini}},t^{\mathrm{LWS}}\right)A_c^0dx}_{\tilde{F}_c^C} & x^{\mathrm{min}}\le x^{\mathrm{ini}}<x^{\mathrm{har}}\\ \underbrace{\int_{t^{f,x^{\mathrm{har}}}}^{t^{s,x^{\mathrm{har}}}}-F_h^V\,dt}_{\tilde{F}_c^V}+\underbrace{\int_{t^{f,x^{\mathrm{har}}}}^{t^{s,x^{\mathrm{har}}}}-F_h^L\,dt}_{\tilde{F}_c^L}+\underbrace{\int_{t^{f,x^{\mathrm{har}}}}^{t^{s,x^{\mathrm{har}}}}-F_h^A\,dt}_{\tilde{F}_c^A}+\underbrace{\int_{-\delta}^{0}s_c\left(x^{\mathrm{ini}},t^{\mathrm{LWS}}\right)A_c^0dx}_{\tilde{F}_c^C} & x^{\mathrm{har}}<x^{\mathrm{ini}}\le x^{\mathrm{max}}\end{cases}. \quad (5)$$

The tidally averaged additional along estuary salt transport at the initial position is then given by $\tilde{F}_c^{\mathrm{trp}}=\Delta\tilde{F}_c^{\mathrm{trp}}/T$, where T is the tidal period. In Equation 5, x^{max} and x^{min} denote the up- and down-estuary limits of the added salt transport and A_c^0 is the tidally averaged cross-sectional area in the main channel. The decomposed instantaneous salt transport components at the harbor entrance (Equation 4) are used to distinguish between contributions to the additional salt transport from the cross-sectionally averaged exchange $\left(F_h^A\right)$ and from exchange processes that are diffusive in nature (i.e.., F_h^V and F_h^L). The first term $\left(\tilde{F}_c^V\right)$ and the second term $\left(\tilde{F}_c^L\right)$ represent the additional salt

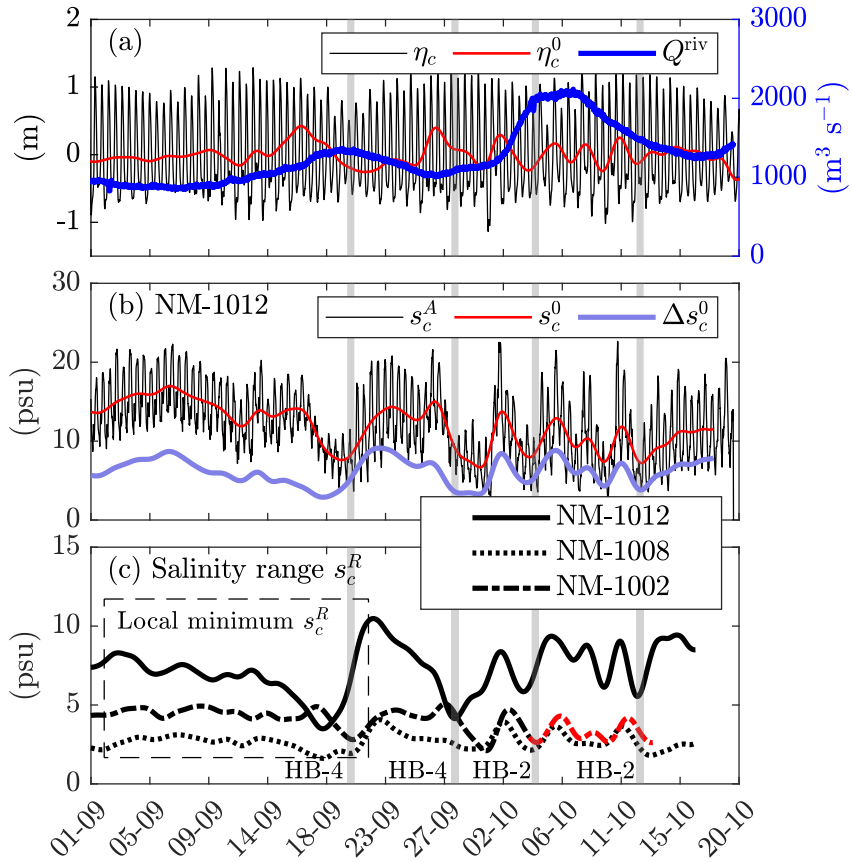

Figure 4. Overview of the hydrodynamic conditions during the measurement campaign. Gray lines indicate the timing of the 13-hr shipboard surveys. (a) Water levels η_c and subtidal water levels η_c^0 near mooring NM-1012, along with freshwater discharge Q^{riv} from the Rhine (the main freshwater source) measured at Lobith (see Figure 1a). (b) Mooring-averaged salinity s_c, subtidal salinity s_c^0, and tidally averaged top-to-bottom salinity difference Δs_c^0 at mooring NM-1012. (c) Salinity range s_c^R derived from salinity at the three moorings in the New Meuse, averaged over the corresponding mooring period (Figure 1). At NM-1002, the period highlighted in red indicates that the salinity signal was clipped. In this context, "clipped" means that during part of the tidal cycle, the measured salinity was equal to that of the river discharge. This influences the estimated tidal salinity range compared to stations where saline water is present throughout the entire tidal cycle.

transport arising from the vertical and lateral structure of the channel–harbor exchange, respectively. The third term $(\tilde{F}_c^A)$ represents the salt transport associated with cross-sectionally averaged exchange over the trap entrance. This term is typically negative when flow in the channel and in the trap are out of phase, as it represents the salt flux arising from particles that are subject to a down-estuary excursion. Furthermore, $\tilde{F}_c^A$ is compensated by the salt transport arising from the up-estuary excursion of the non-trapped volumes, which is typically positive and represented by compensating term $\tilde{F}_c^C$.

To track when the control plane crosses the trap, the demeaned tidal discharge component at a cross-section just down-estuary of the evaluated harbor, Q_c^1, is used. By integrating the cumulative transport, $\int_0^t Q_c^1, \mathrm{d}t$, we determine the two moments at which the upstream volume relative to the cross-section is equal, corresponding to the times when the control plane, which has departed from x^{ini}, passes the trap. These times are denoted by $t^{\mathrm{f},x^{\mathrm{har}}}$ and $t^{\mathrm{s},x^{\mathrm{har}}}$. The relative distance from the harbor $x^{\mathrm{har}} - x^{\mathrm{ini}} \approx \frac{1}{A_c^0}\int_0^t Q_c^1, \mathrm{d}t$ is estimated from the volume that has passed through the cross-section divided by the tidally averaged cross-sectional area A_c^0. Furthermore, in our analysis, we evaluate the period between two consecutive low-water slacks in the harbor (i.e., $t = 0$ corresponds to low-water slack in the trap).

The net displacement δ in the integral in Equation 5 is obtained from the net discharge from the harbor, Q_h, during the evaluated period:

$$\delta\left(x^{\mathrm{ini}}\right) = \int_{t^{\mathrm{f},x^{\mathrm{har}}}}^{t^{\mathrm{s},x^{\mathrm{har}}}} Q_h dt / A_c^0 \tag{6}$$

where the integral is analogous to the third term, but for the exchange of volume. Similarly, following the reasoning used to determine the crossing times of the control plane, we estimate $s_c\left(x^{\mathrm{ini}}, t_{\mathrm{LWS}}\right)$ from the cross-sectionally averaged salinity signal in the main channel, immediately in front of the harbor.

Through Equation 5, the additional salt transport resulting from tidal trapping can be estimated for an individual trap (Dronkers, 1978; Van Keulen et al., 2025). In essence, Equation 5 quantifies the redistribution of salt water arising from the phasing and asymmetry of channel–trap exchange relative to the tidal excursion. A limitation of this approach is that it evaluates only the local balance, without explicitly accounting for variations along the tidal excursion length. Moreover, Equation 5 quantifies the additional salt transport of a single harbor. In this study, Equation 5 is applied to assess the potential contribution of different harbors and to identify spatial differences between them (Section 4.3), and to obtain a parameterization of its main effect (also see Section 5 and Appendix B).

3. Observations of Exchange Between Channel and Harbor

3.1. Hydrodynamics Conditions

Figure 4 shows the hydrodynamic conditions during the field campaign, with the 13-hr surveys highlighted in gray. The Rhine discharge was low during the first half of the campaign ($850 < Q^{\mathrm{riv}} < 1350$ m^3/s), but increased during the second half (Figure 4a). This increase led to an overall reduction in the measured salt concentrations in the NM (Figure 4b). The conditions during the 13-hr surveys were characterized by a non-stationary salinity field, with subtidal salinity concentrations temporarily decreasing during the observation period. Figure 4c shows the observed tidal salinity range s_c^R (i.e., salinity variation over a tidal cycle) at three mooring locations. During the first half of the campaign (when Q^{riv} was relatively low), the salinity range shows a clear minimum at NM-1008, compared to NM-1012 (down-estuary) and NM-1002 (up-estuary). In Sections 3 and 4, we show that this local minimum in s_c^R strongly influences the nearby salt exchange between the channel and the harbors.

3.2. Observed Flow and Salinity in the Main Channel

Figure 5 presents the measured along-channel velocities and salinity at transect W-W′, located down-estuary of the harbors (see Figures 1d and 1e). The barotropic tide is characterized by strong tidal distortion (see Figures 5a–5d), which is reflected in both the large amplitude ratio $A_c^{\mathrm{ratio}} = \hat{\eta}_c^{M_4}/\hat{\eta}_c^{M_2} \approx 0.22$ and the phase difference $\Delta\theta = 2\theta_c^{M_2} - \theta_c^{M_4} \approx 10°$ between the quarter-diurnal and semi-diurnal components. The relative large amplitude ratio $\left(A_c^{\mathrm{ratio}}\right)$ and the phase difference $(\Delta\theta_c)$ close to zero results in nearly equal durations of flood and ebb, with the quarter-diurnal component amplifying high water (HW) and reducing low water levels.

For the semi-diurnal M_2 tidal constituent, the phasing of the horizontal tide $\left(\theta_c^{U_2}\right)$ leads the vertical tide $\left(\theta_c^{M_2}\right)$ by approximately 45°. The combination of the observed tidal distortion and the phase difference between the horizontal and vertical tides produces a relatively short and intense flood current (Figures 5e–5h). This phase difference between the vertical and horizontal tide in the main channel is substantially smaller than the maximum velocity phase lead of 90° expected for a purely standing wave, a short basin, or a strongly convergent channel (Friedrichs, 2010). Consequently, since harbors act as short basins, the velocity phase lead in the harbor to the current in the main channel, $\theta_c^{U_2} - \theta_h^{U_2}$, must be close to 45°. Because of this phase difference, there is potential for a substantial contribution of tidal trapping through advective out-of-phase exchange (Dronkers, 1978; Van Keulen et al., 2025). The contribution of out-of-phase exchange is further quantified in Section 4.3.

Panels i through l in Figure 5 summarize the observed salinity dynamics. The most important observations are the weaker intertidal salinity variations at HB-4 compared to HB-2, in line with the results of the nearby moorings (Figure 4c). The stronger intertidal variations at the HB-2 Harbor are most pronounced in near-bed salinity, s_c^{bed}. However, direct comparisons are difficult, since conditions varied between the four surveys (Figure 4). Furthermore, at HB-2, the passage of relatively low-salinity water is observed during early flood, reducing the near-surface salinity $\left(s_c^{\mathrm{sur}}\right)$. This drop in the near-surface salinity is explained by inflow from the Old Meuse (OM),

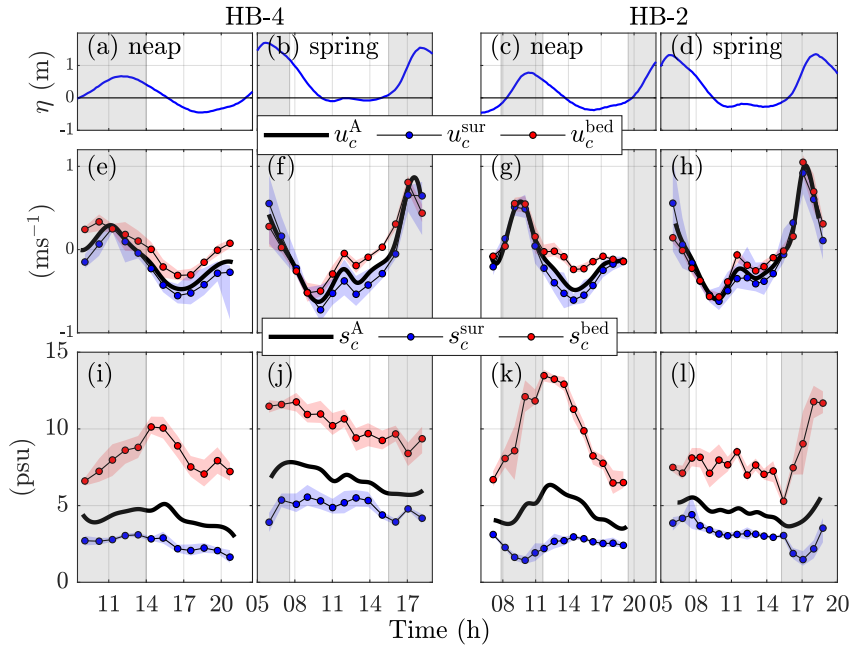

Figure 5. Observations in the main channel at transect W–W′ (located down-estuary of the harbors) during the 13-hr surveys. Panels (a–d) present water-level variations obtained from the nearby tide gauge. Panels (e–h) show the cross-sectionally averaged along-channel velocity (u_c^A), the near-surface velocity (u_c^{sur}), and the near-bottom velocity (u_c^{bed}). The near-surface and near-bottom properties represent the average over the near-surface 4 m and the lowermost 4 m of the water column. Panels (i–j) display the corresponding salinity fields. Lateral variations of the near-surface and near-bottom properties are indicated by red and blue shading, respectively.

which is at that time still in the ebb phase. The mechanism behind this type of channel interaction is discussed in detail by Warner et al. (2002).

For the monitored cross-sections during the 13-hr surveys, the salt balance has been derived (see appendix A2). Analysis of the subtidal salt transport showed that during all 13-hr surveys there was a net seaward export of salt in the main channel, as well as a net export of salt from the harbors into the main channel. We attribute this seaward export partly to subtidal water-level variations during the campaigns and partly to increased river discharge during some of the 13-hr surveys (Figure 4a). Up-estuary transport of salt is mostly governed by the steady shear contribution, $F_c^{st,shear}$, whereas the contribution of the tidal oscillatory flux, F_c^{tide}, is small or even negative.

3.3. Observed Flow and Salinity (Structure) Near the Harbor Entrance

Harbors often exhibit a lock-exchange-like flow driven by density dynamics (Abraham et al., 1986; De Nijs et al., 2009; Roelfzema & Van Os, 1978; van Maren et al., 2009). Figures 6 and 7 show the observed along-harbor velocity structure, at HB-2 and HB-4 respectively. We focus on the transects collected around HW during the two neap-tide surveys, as they most clearly reveal the differences between the two harbors. The corresponding depth-averaged density differences between the CTD casts in the harbor and the main channel and are shown in Figure 8.

At HB-2 (Figure 6), the flow and salinity fields reveal a typical lock-exchange-like flow that reverses direction throughout the tidal cycle. At the start of the flood (tracks 1–3), the near-bed current is directed toward the main channel. This current is driven by the higher density in the harbor (panel a in Figure 8). Around HW (track 4), the direction of the vertically sheared flow reverses as salinity in the main channel increases with the incoming tide. This is also reflected in the fact that the depth-averaged density difference, $\Delta\overline{\rho}_{H-H'}$, reverses sign during mid-flood. The vertically sheared flow, with near-bottom currents directed toward the harbor, is maintained throughout tracks 5–8 (track 8 not shown). During the main channel ebb (tracks 9–14, not shown), the vertically sheared flow reverses direction again, due to the reduction in main-channel salinity caused by the ebb current. In addition, the flow structure near the head of the harbors is locally influenced by eddies (see Figure 6, tracks 3–4).

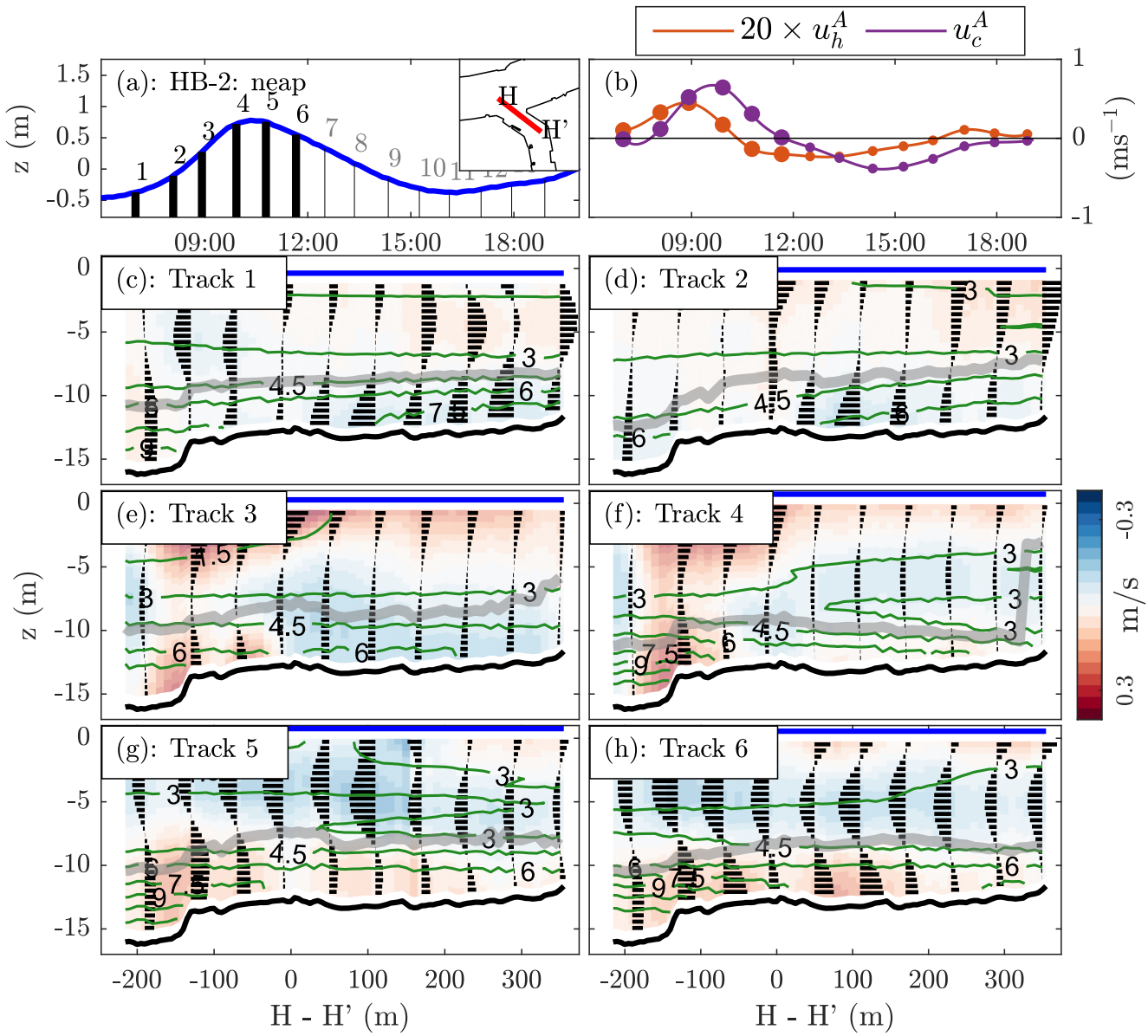

Figure 6. Along-harbor velocity and salinity structure at transect H–H′ at HB-2 during the neap tide (Figure 1c). (a) Moment within the tidal cycle at which each transect was taken. Transects shown in Panels (c)–(h) are indicated with a thick vertical line. (b) Along-channel $\left(u_c^A\right)$ and along-harbor $\left(u_c^H\right)$ velocity components. Larger scatter points are used to highlight the tracks shown in Panels (c)–(h). (c)–(h) Along-harbor velocity component indicated by color and arrows. The green contour lines indicate salinity. The thick gray line indicates the approximate height of the pycnocline, estimated by fitting a sigmoid function to the vertical salinity profiles (Niesten et al., 2024).

At HB-4 (Figure 7), a three-layered vertically sheared structure dominated the current profiles for most of the tide, deviating from the classical two-layered profile. During the early flood (tracks 1–2), both near-bottom and surface flows enter the harbor, with a mid-column outflow. This near-bed inflow contrasts with the velocity structure at HB-2 and is unexpected, given the higher depth averaged density in the harbor (Figure 8c). Near HW (tracks 3–4), the flow transitions to the expected two-layer structure, with the near-bed current directed toward the main channel. After HW (tracks 5–6), a near-bed current toward the harbor re-develops, accompanied by a notable increase in salinity in the lower part of the water column. However, a two-layered vertically sheared flow profile does not form, as a near-surface flow toward the harbor is maintained. The near-bed current persists up to track 7. For the remaining tracks (not shown), the flow returns to a vertical structure characterized by mid-column outflow and near-surface inflow.

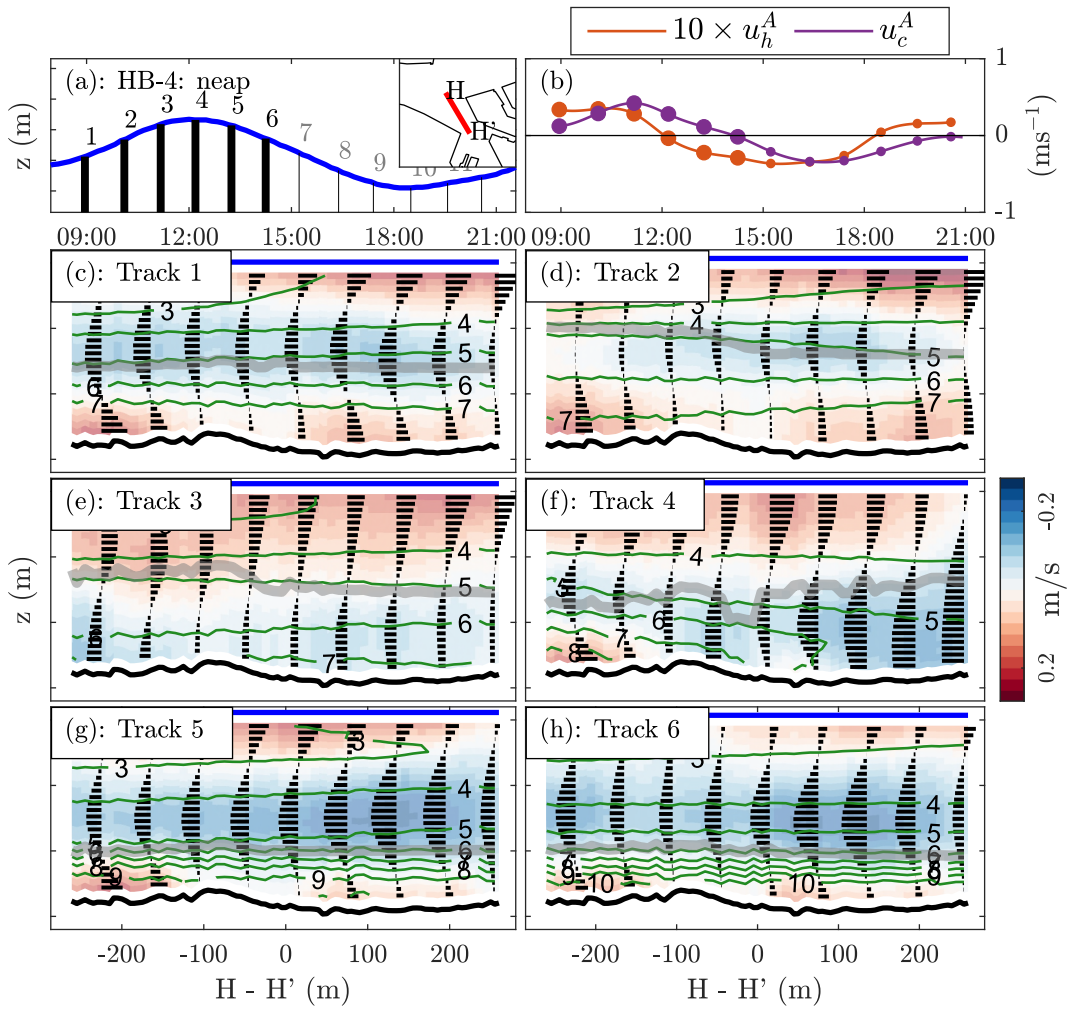

Figure 7. Same as Figure 6, but for HB-4 during the neap tide survey.

3.4. Analysis of Observed Flow Structures in the Harbors

In the following sections, (a) the extent to which the observed vertically sheared flow is driven by density dynamics is quantified, and (b) an explanation for the mid-column outflow observed at HB-4 is provided.

3.4.1. Explanation of Inter-Tidal Flow Structure and Density Dynamics

Channel-harbor salt exchange is often assumed to be driven by gravitational dynamics. To validate this assumption and assess the role of density-driven tidal trapping, we follow the analysis of W. Geyer et al. (2024). First, the composite Froude number for a two-layer regime, G, is calculated for the flow in the harbor (Armi & Farmer, 1986):

$$G = \left[\frac{\left(u_h^{\text{top}}\right)^2}{g' h_h^{\text{top}}} + \frac{\left(u_h^{\text{bot}}\right)^2}{g' h_h^{\text{bot}}} \right]^{1/2}, \tag{7}$$

where h_h^{top} and h_h^{bot} denote the depths of the top and bottom layers, respectively. Here, the level of the interface between the two layers is based on the expected location of the pycnocline (gray lines in Figures 6 and 7), u_h^{top} and u_h^{bot} are the layer-averaged velocity in the top and bottom layer (respectively) and $g' = \left(\frac{\rho^{\text{bot}} - \rho^{\text{top}}}{\bar{\rho}}\right) g$ denotes reduced density. Again, the densities ρ^{top} and ρ^{bot} are layer-averaged properties. Second, we compare G as a

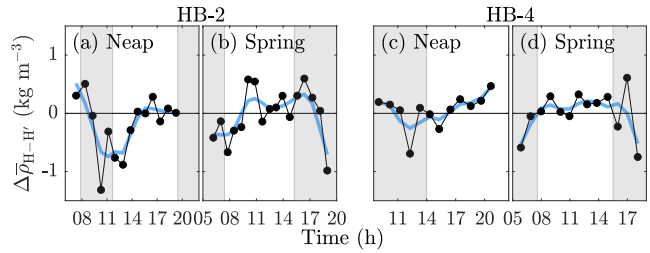

Figure 8. Depth-averaged density difference $\left(\Delta\overline{\rho}_{H-H'}\right)$ calculated from the vertical CTD casts taken at transect H–H′. Positive values indicate a higher depth-averaged density in the harbor. The light-blue line shows the smoothed depth-averaged density difference obtained using a LOWESS filter with a span of 0.3. Gray shading indicates the duration of the horizontal flood period.

function of the fractional depth of the bottom layer (the active layer) $h'_h = \left(\frac{h_h^{bot}}{h_h^{top}+h_h^{bot}}\right)$, and compare it with the composite Froude number obtained using the Benjamin (1968) solution for density currents (G_{Ben}), as derived by W. Geyer et al. (2024):

$$G_{Ben} = \left[\frac{h'_h(2-h'_h)}{(1-h'_h)(1-h'_h)^2}\right]^{1/2}. \tag{8}$$

This analysis allows to assess to what extent the observed flow is consistent with density-driven dynamics.

Figure 9 presents G against the fractional depth h'_h for the tracks in Figures 6 and 7. For HB-2, G aligns with the Benjamin (1968) analytical solution for G_{Ben} for most of the tracks. Only for tracks 3 and 4 this is not the case; these tracks cover the period during which the density current reverses direction. For HB-4, tracks 1 and 2, G deviates from G_B. These two tracks were characterized by a three-layered flow structure and a weak horizontal density gradient. For tracks 3 and 4, a two-layer flow developed and G aligns with G_{Ben}. An agreement with G_{Ben} is also obtained for tracks 5 and 6, during which a near-bed density current developed that intruded into the harbor (although the upper layer was not strictly uniform for those tracks).

The agreement between the composite Froude number and the solution by Benjamin (1968) indicates that the vertical flow structure results from density-driven dynamics. However, during the reversal of the density current at HB-2 and for the tracks at HB-4 that were characterized by a three-layered profile, the observations did not align with the theoretical solution. In the next section, the three-layered profile is further investigated.

3.4.2. Explanation for the Observed Mid-Depth Outflow at HB-4

At HB-4, a persistent mid-depth flow reversal was observed (Figure 7). This coincided with stronger vertical stratification in the harbor compared to the main channel. We examine whether this gradient in vertical stratification can account for the observed three-layered vertically sheared flow profile. We do this by calculating the vertical profile of the residual current that would arise from the balance between the pressure gradient and frictional forces, in a flow that is subject to a depth-varying lateral density gradient (Nunes & Simpson, 1985):

$$u(z) = \frac{g}{\overline{\rho}A_z}\left(\frac{3}{2H^3}\left(I_4^H + HI_3^H\right)\left(z^2+H^2\right) - \left(I_3^z + I_3^H\right)\right), \tag{9}$$

Herein, g is the gravitational acceleration, $\bar{\rho}$ the depth averaged density (denoted by the over-bar $\bar{\cdot}$), A_z is the vertical eddy viscosity, H is the water depth, and z is the vertical coordinate (positive upwards). In Equation 9, I_n^z is defined as:

$$I_n^z = \int_0^z \int_0^z .. \int_0^z \frac{\partial \rho}{\partial y} dz_1 .. dz_{n-1} dz_n, \tag{10}$$

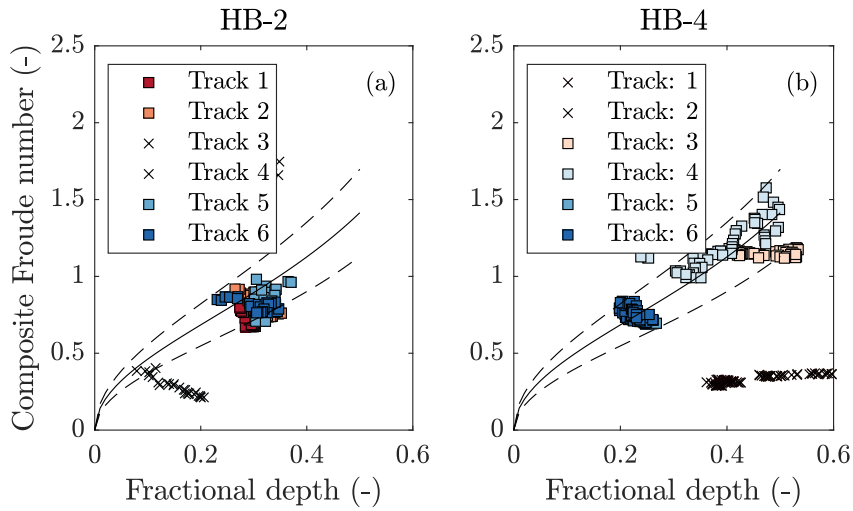

Figure 9. Composite Froude numbers (G) as a function of fractional depth. (a) Results for the HB-2 neap-tide survey for the tracks shown in Figure 6. (b) Same as (a), but for the HB-4 neap-tide survey for the tracks shown in Figure 7.

where I^H indicates that the integral is evaluated up to $z = -H$, and y indicates the direction perpendicular to the main channel (or along the channel in the harbor). For a depth-uniform horizontal density gradient, Equation 9 reduces to the classical expression for gravitational circulation (Hansen & Rattray, 1965) or transverse velocity (Nunes & Simpson, 1985). To investigate the influence of horizontal differences in the vertical stratification, we decompose the tidal-mean horizontal density gradient into a component that is both tidally and depth averaged, $\langle\overline{\rho}_y\rangle$, and a component that is tidally averaged but varies with depth, $\langle\rho'_y\rangle$. Here, the operator $\langle\cdot\rangle$ denotes a tidal average. Subsequently, these properties are used to obtain a current profile, Equation 9, which is governed by $\langle\overline{\rho}_y\rangle$ and $\langle\rho'_y\rangle$. Here, the horizontal stratification gradient is expressed through the gradient in the potential energy anomaly Φ_y, with the potential energy anomaly defined as $\Phi = -g\int_{-H}^{\eta}\rho'_y z dz$ (Simpson et al., 1990).

Figure 10 illustrates the baroclinic pressure–induced acceleration and the corresponding current profiles driven by Φ_y in panels a and b, alongside the well-known profiles resulting from $\langle\overline{\rho}_y\rangle$. The results are obtained for idealized density configurations with either a depth-averaged horizontal density gradient or a density gradient that varies linearly with depth, reverses sign, and has a depth-average equal to zero. Panel c shows the baroclinic pressure–induced acceleration calculated from the observed tidally averaged density gradient, $\langle\rho_{\mathrm{H–H'}}\rangle$, obtained from the CTD profiles at transect H–H′ during the neap-tide survey at HB-4. The tidally and depth-averaged contribution $\langle\overline{\rho}_{\mathrm{H–H'}}\rangle$ was nearly zero, but, as indicated, stratification of the water column was significantly stronger in the channel, resulting in $\Phi_{\mathrm{H-H'}}$ being positive. In the absence of a depth-averaged density gradient, but in the presence of a horizontal stratification gradient, the baroclinic acceleration peaks at mid-depth and vanishes near the bottom. Panel d of Figure 10 compares the observed tidally averaged residual current profile with that predicted by Equation 9, using the observed profiles of $\langle\rho_{\mathrm{H–H'}}\rangle$. To match the observed current magnitude, A_z was set to 0.003 $\mathrm{m^2/s}$, which is similar to the value found by Biemond et al. (2025). The current profile resulting from $\langle\Phi_{\mathrm{H–H'}}\rangle$ exhibits a pronounced outflow at mid-depth and inflow near the surface, as observed. Therefore, we attribute the observed mid-depth outflow and surface inflow—present throughout nearly the entire tidal cycle—to stronger stratification in the main channel compared to the harbor.

3.5. Analysis of Instantaneous Channel–Harbor Salt Exchange

To investigate whether the mechanisms of salt exchange differ between the two harbors, we quantify the instantaneous channel–harbor salt exchange and the contributions of different exchange processes. Specifically, we decompose the instantaneous salt transport observed at transect Z–Z′ using Equation 4 to quantify the contributions from tidal filling and emptying, as well as the exchange of salt that is diffusive in nature (Figure 11).

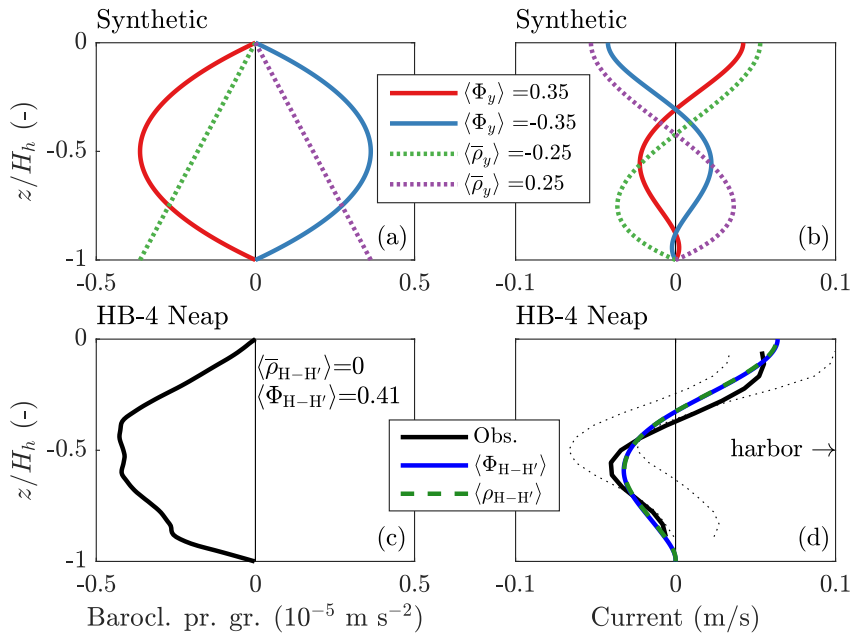

Figure 10. Influence of the difference in stratification between the main channel and the harbor on the residual currents observed near the harbor entrance of HB-4 during the neap-tide survey. (a) Synthetical profiles of depth-averaged density $(\overline{\rho}_y)$ and stratification (Φ_y), based on either a constant horizontal density gradient or a linearly varying horizontal density gradient over depth, with a zero depth-averaged mean. (b) Flow velocity profiles calculated corresponding to conditions in panel (a) using Equation 9. (c) Profile of the baroclinic pressure gradient calculated from the tidally averaged density gradient $(\langle\rho_{\mathrm{H-H'}}\rangle)$ at the along-harbor transect H–H′ at HB-4. (d) Observed tidally averaged velocity profile, compared with velocity profiles calculated using Equation 9 with the measured density gradient $\langle\rho_{\mathrm{H-H'}}\rangle$ or the stratification gradient $(\langle\Phi_{\mathrm{H-H'}}\rangle)$. A vertical eddy viscosity of $A_z = 0.003$ m^2/s is used for the calculations. Dashed lines indicate the velocity profiles around peak flood and ebb.

The instantaneous salt transport resulting from the cross-sectionally averaged current and salinity $\left(F_h^A\right)$, which reflects the salt transport due to filling and emptying of the harbor, dominates the total instantaneous salt transport for both harbors (compare Figures 11e–11h with Figures 11a–11d). This transport can be further decomposed into two components: the instantaneous cross-sectionally averaged salt transport associated with the tidally averaged salinity, and the transport associated with the deviation from the tidal mean. This yields

$$F_h^A = F_h^{\mathrm{st,A}} + F_h^{\mathrm{var,A}} = u_h^A\langle s_h^A\rangle + u_h^A\left(s_h^A - \langle s_h^A\rangle\right), \tag{11}$$

where $\langle\cdot\rangle$ denotes a tidal average. Evaluating both terms shows that the contribution of F_h^A is predominantly determined by the exchange of water with salinity equal to the tidal average $\left(F_h^{\mathrm{st,A}}\right)$, whereas the contribution from inter-tidal salinity variations $\left(F_h^{\mathrm{var,A}}\right)$ is an orders of magnitude smaller (compare panels e–h in Figure 11 with panels a–d). This implies that the change in salt concentration due to filling and emptying is small.

For the salt transport that is diffusive in nature, the contribution of the laterally sheared salt flux in the along-channel direction of the harbor, F_h^L, was found to be small. Note that F_h^L was assessed from the CTD casts taken at transect Z–Z′ only for HB-4 (Figure 1e). This limited contribution arises because the observed lateral salinity differences were small, despite the presence of lateral variation in the current field (mostly in near-surface currents). In contrast, the exchange associated with the instantaneous vertically sheared salt transport $\left(F_h^V\right)$ is substantially larger compared to F_h^L and $F_h^{\mathrm{var,A}}$.

At HB-2, F_h^V is directed into the harbor (positive) from approximately HWS – 2h to HWS + 2h, consistent with the observed density current dynamics (Figure 6). Compared to HB-4, the observed variations in F_h^V at HB-2 are larger, particularly during the neap-tide surveys. At HB-4, the contribution from the vertical structure $\left(F_h^V\right)$ is on average directed seawards (negative) during both surveys and exhibits relatively weak inter-tidal variability,

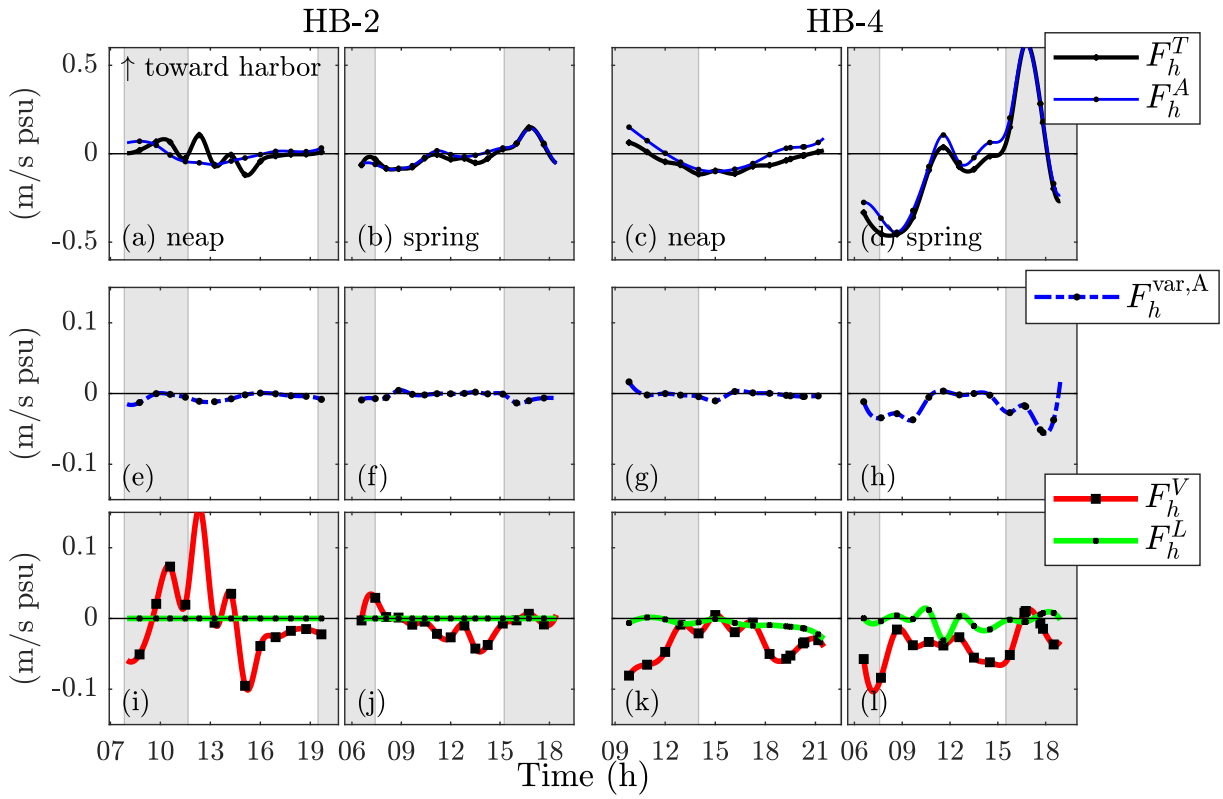

Figure 11. Instantaneous salt transport observed at the harbor entrance (transect Z–Z′) during the 13-hr surveys at HB-2 and HB-4. Positive values denote transport directed into the harbor. (a–d) Total instantaneous salt transport $\left(F_h^T\right)$ and the salt transport associated with barotropic filling and emptying $\left(F_h^A\right)$. (e–h) Contribution to the salt transport associated with the cross-sectionally averaged current and tidally varying salinity $\left(F_h^{\mathrm{var,A}}\right)$. (i–l) Instantaneous salt transport associated with vertically $\left(F_h^V\right)$ and laterally $\left(F_h^L\right)$ sheared salt transport, both considered diffusive in nature. Gray shading indicates horizontal flood in the main channel.

which we attribute to the smaller salinity range (Figures 4 and 5). The net seaward salt transport toward the main channel at HB-4 is consistent with the salt balance being unsteady during the 13-hr measurement (see Appendix A2). Its more pronounced influence on the dynamics at HB-4 aligns with the analysis of the relative importance of subtidal exchange compared to tidal trapping (this is further discussed in Section 4.4).

4. Generalization From Numerical Modeling

We further investigate the harbor-channel exchange and its effect on salinity dispersion with the numerical model. Section 4.1 is mainly focused on the salinity range variation along the estuary, which plays a key role in the harbor contribution to salt dispersion. In Section 4.2, we examine the channel-harbor salt exchange for the larger harbors (Figure 1) and relate differences in exchange to the local minimum in salinity range. This is followed by the quantification of the effect of tidal trapping on the dispersion of salt in the main channel (Section 4.3). In Section 4.4, we compare the additional salt transport from tidal trapping to that associated with subtidal exchange between the channel and the harbor.

4.1. Subtidal Salt Transport and the Minimum in Salinity Range

Figure 12a presents the subtidal salt fluxes in the main channel, as determined from the simulations mentioned in Section 2.3, following the decomposition outlined in Appendix A1. The up-estuary directed transport contributions are shown as a fraction of the salt transport associated with flushing by the river discharge $\left(F_c^i/F_c^{\mathrm{res}}\right)$. This fraction is known as the diffusive salt fraction (Hansen & Rattray, 1966). Flushing by the river discharge $\left(F_c^{\mathrm{res}}\right)$ is primarily balanced by the transport related to the steady shear flux, $F_c^{\mathrm{st,shear}}$, throughout most of the domain. The transport due to the tidal oscillatory flux, F_c^{tide}, which incorporates the effects of tidal trapping, becomes the

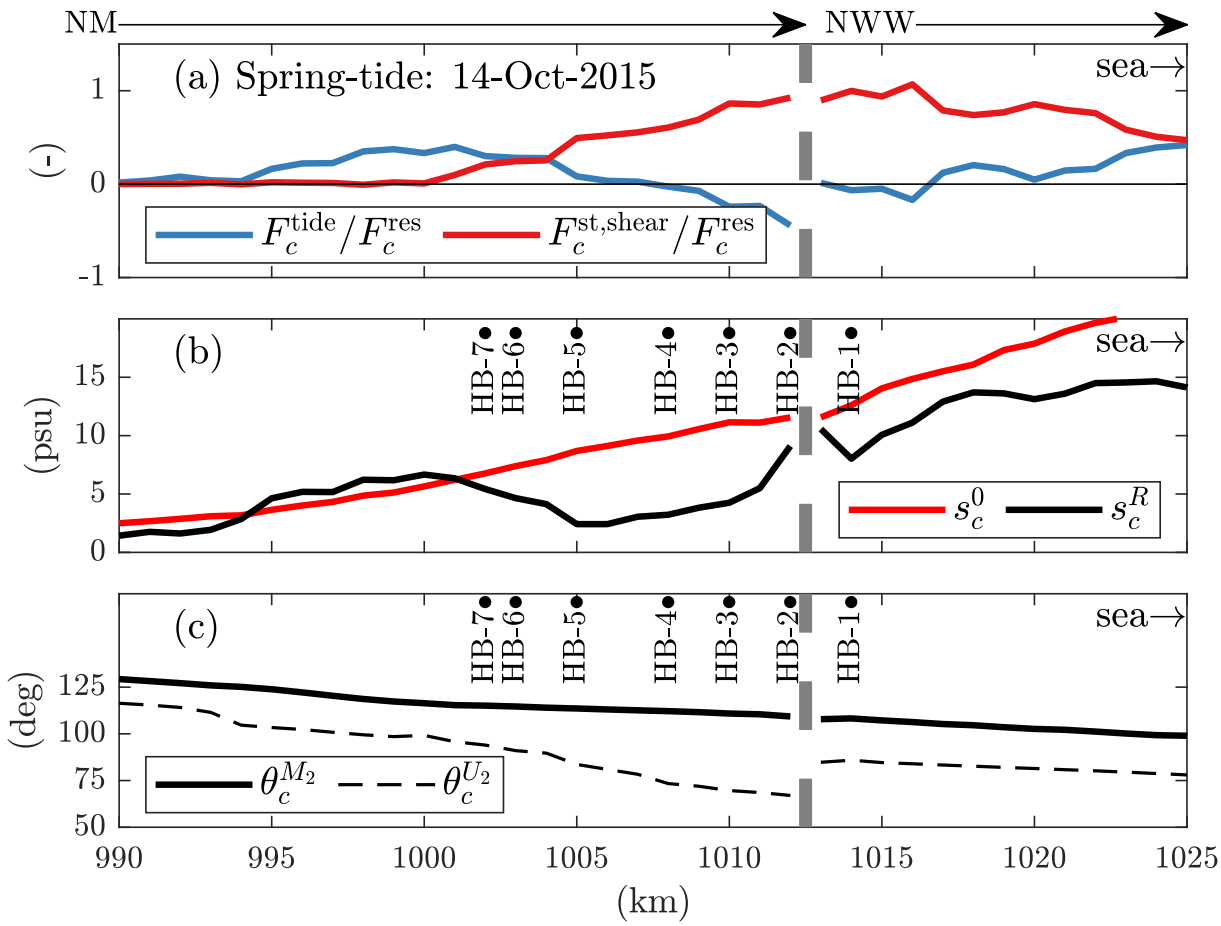

Figure 12. Overview of the modeled estuarine conditions near spring tide (14-10-2015). (a) Dominant components of the subtidal salt transport: the tidal oscillatory salt contribution $\left(F_c^{\text{tide}}\right)$ and the contribution from steady shear $\left(F_c^{\text{st,shear}}\right)$. Along-channel salt transport contributions are expressed as a diffusive salt fraction, F_c^i/F_c^{res}, where F_c^{res} represents flushing driven by river discharge. (b) Subtidal salinity s_c^0 and the tidal salinity range s_c^R. The tidal salinity range exhibits a local minimum between HB-4 and HB-5. (c) Phasing of the vertical tide $\left(\theta_c^{M_2}\right)$ and horizontal tide $\left(\theta_c^{U_2}\right)$ based on the dominant M_2 tidal constituent. The thick gray dashed line marks the location of the junction between the New Waterway (NWW), the New Meuse, and the Old Meuse.

dominant term upstream of km 1,005. This transition is consistent with findings by W. Kranenburg et al. (2022), Dijkstra et al. (2022) and Biemond et al. (2025). Note that upstream of the junction (indicated by the thick gray dashed line), the tidal oscillatory contribution is negative, consistent with the subtidal salt transport derived from the 13-hr shipboard survey (Appendix A2). This is partly due to the import of relatively low-salinity water from the OM (see Figure 5), but it is expected to also be strongly influenced by changes in channel depth further up-estuary (km 1,002), which we address in a follow-up paper.

Consistent with the field observations during lower discharge conditions (Figure 4), the model results show a local minimum in the tidal salinity range, s_c^R, with the lowest values occurring near HB-4 and HB-5. How this minimum influences the instantaneous channel-harbor salt exchange is explored in the next section. Furthermore, this minimum is not caused by the harbors themselves, as confirmed by exploratory model experiments in which the harbors were removed (data not shown). A potential explanation for the increase in s_c^R in the upper part of the New-Meuse to a sharp increase in channel depth occurring down-estuary of km 1,002, allowing the formations of fronts and the creation of sharp gradient in the along channel salinity structure (Corlett & Geyer, 2020; W. R. Geyer & Ralston, 2015).

Panel c in Figure 12 shows the phasing of the M_2 constituent for both the vertical tide $\left(\theta_c^{M_2}\right)$ and the horizontal tide $\left(\theta_c^{U_2}\right)$ in the main channel. The potential up-estuary salt transport due to advective out-of-phase exchange

depends on the velocity phase difference between the currents in the main channel and the harbor (Dronkers, 1978; Van Keulen et al., 2025). This velocity phase difference is close to $\theta_c^{U_2} - \theta_h^{U_2} \approx \theta_c^{U_2} - \left(\theta_c^{M_2} - 90°\right)$, since the current in the trap is approximately 90° out of phase with the surface elevation due to the short basin length (Friedrichs, 2010). Just up-estuary of the junction, the phase difference between the horizontal and vertical tides is largest (about 42°), implying a smaller channel-harbor velocity phase difference for the adjacent harbors. Further up-estuary, $\theta_c^{U_2} - \theta_h^{U_2}$ decreases (to about 20° at HB-7), leading to an increased channel-harbor velocity phase difference. Hence, a significant contribution from advective out-of-phase exchange is possible based on the phase difference, especially for the more up-estuary harbors; this is further examined in Section 4.3.

4.2. Relation Between Instantaneous Channel-Harbor Salt Exchange and the Salinity Range

The relationship between the instantaneous channel-harbor exchange from vertical shearing and the salinity range in the main channel is further explored in Figure 13.

We first examine the instantaneous salt transport, decomposed through Equation 4, for the different harbors, normalized by the absolute maximum value of total instantaneous salt transport F_h^T (Figures 13a–13f). The relative contribution of the transport F_h^V due to the vertically sheared flow is clearly the smallest at HB-4 and HB-5, where s_c^R is small (see Figure 12). This local reduction in the transport contributions thar are diffusive in nature is further highlighted by an increase in the ratio $R = \langle |F_h^A| \rangle / \left(\langle |F_h^V| \rangle + \langle |F_h^L| \rangle \right)$ (Figure 13h).

To understand the relationship between F_h^V and s_c^R, we consider a first-order approximation of the maximum salt transport associated with a salt flux resulting from a density-driven, two-layer sheared flow (Benjamin, 1968; C. Kranenburg, 1996). For the case of an arrested front, where the flow in the passive (lower) layer has reduced to zero, Benjamin (1968) obtained the solution $\frac{U_u}{g'H} = \frac{1}{4}$, where U_u is the velocity upstream of the front and H is the depth. When we assume equal depths for the top and bottom layers and approximate the density difference from s_c^R as $\Delta\rho = \rho_0 \beta s_c^R$ (van Maren et al., 2009), we can define the following properties to assess the instantaneous salt transport associated with vertically sheared flow resulting from fronts in the harbors:

$$
\begin{aligned}
u^{\text{top}} &= -\frac{1}{2}\sqrt{\frac{\rho_0 \beta s_c^R}{\overline{\rho}}\, g H_h}, & u^{\text{bot}} &= \frac{1}{2}\sqrt{\frac{\rho_0 \beta s_c^R}{\overline{\rho}}\, g H_h}, \\
q^{\text{top}} &= -\frac{1}{4} H_h \sqrt{\frac{\rho_0 \beta s_c^R}{\overline{\rho}}\, g H_h}, & q^{\text{bot}} &= \frac{1}{4} H_h \sqrt{\frac{\rho_0 \beta s_c^R}{\overline{\rho}}\, g H_h}, \\
s^{\text{top}} &= s_h^A - \frac{1}{2} s_c^R, & s^{\text{bot}} &= s_h^A + \frac{1}{2} s_c^R.
\end{aligned}
\tag{12}
$$

where H_h is the depth of the harbor and the superscripts $^{\text{top}}$ and $^{\text{bot}}$ indicate the upper and lower layers, respectively. The magnitude of the salt transport for this two-layer flow, based on Equation 12, is given by:

$$
\hat{F}_h^V = q^{\text{top}} s^{\text{top}} + q^{\text{bot}} s^{\text{bot}} = \frac{1}{4} (\beta g)^{1/2} \left(s_c^R H_h \right)^{3/2} B_h, \tag{13}
$$

with B_h the width of the harbor entrance and $\frac{\rho_0}{\overline{\rho}} \approx 1$. Note that the positive x-direction is defined as pointing into the harbor. Equation 13 indicates that the salt transport from the exchange caused by vertical shearing scales with the salinity range as $\hat{F}_h^V \propto \left(s_c^R\right)^{3/2}$.

Equation 13 assumes that the instantaneous salt transport associated with vertical variations is driven solely by density differences, and neglects the contribution from the depth-averaged current generated by the periodic filling and emptying of the basins. Since the depth-averaged currents are typically an order of magnitude smaller due to the large depth of the basin, this contribution is expected to be small.

In panel i of Figure 13, the root of the tide-averaged squared salt transport from vertical shearing per unit width $\sqrt{\left\langle \left(\overline{u_h^V s_h^V} \right)^2 \right\rangle}$ as computed from the model results, is plotted against the tidal salinity range s_c^R in front of the

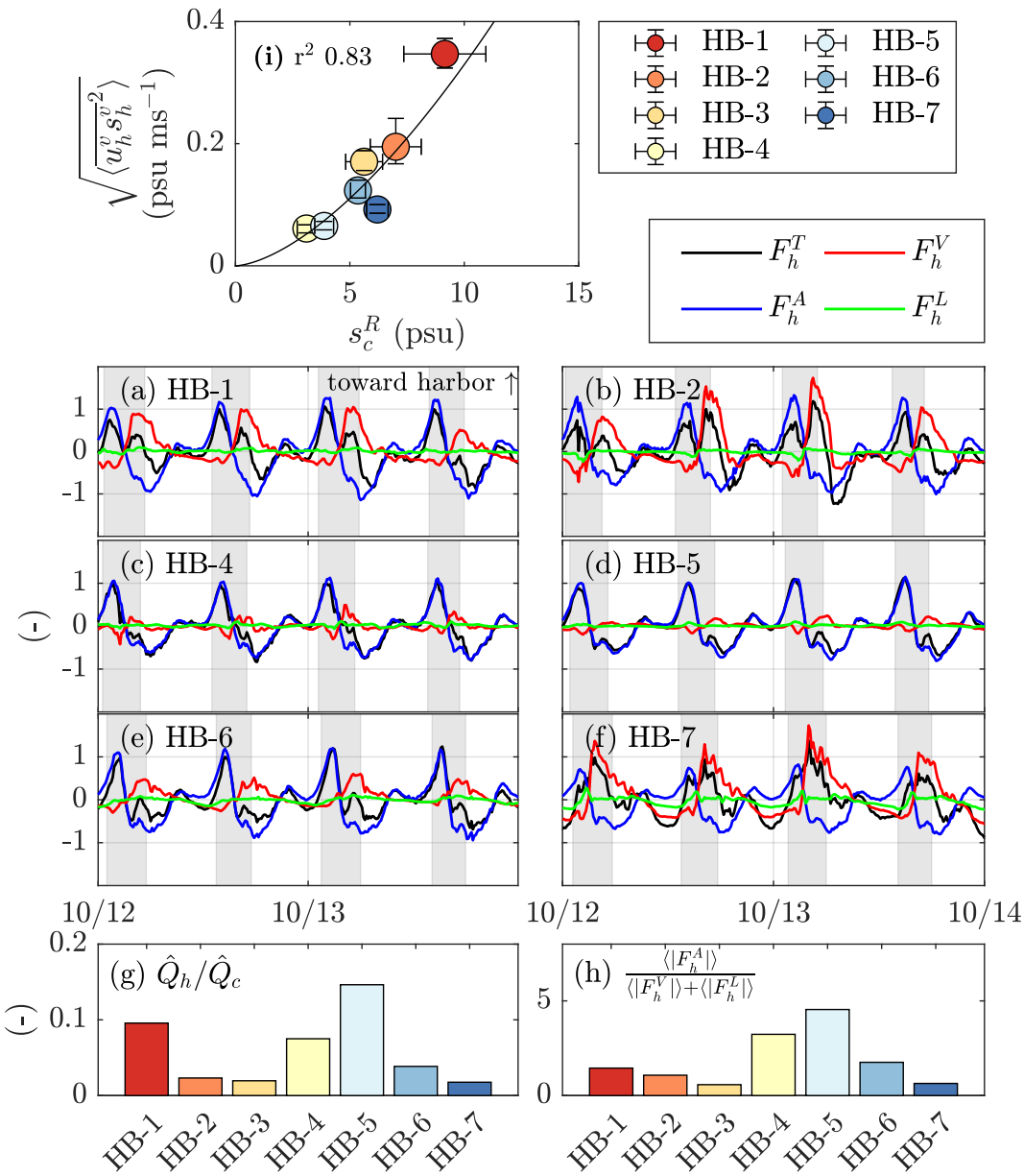

Figure 13. Overview of the modeled instantaneous exchange of salt between the channel and the harbors. (a–c). Normalized instantaneous decomposed salt transport contributions for different harbors, derived from Equation 4. The salt transport contributions are normalized by the absolute maximum value for the period shown $(F_h^i/\max(|F_h^T|))$. The gray shaded background shows the cross-sectionally averaged flood associated with the horizontal tide in the main channel. (g) Relative size of the harbor, based on the ratio between the discharge amplitude at the harbor entrance $\hat{Q}_h$ and the discharge amplitude in the main channel $\hat{Q}_c$. (h) Ratio between the absolute tide-averaged advective exchange $\langle|F_h^A|\rangle$ and the absolute tide-averaged diffusive exchange $\langle|F_h^V|\rangle + \langle|F_h^L|\rangle$. (i) Relation between the salinity range s_c^R and the squared, tide-averaged salt flux from vertical shearing per unit width $\sqrt{\langle\overline{u_c^V s_c^V}\rangle^2}$. The black line represents a power-law fit to the data of the form $y = \alpha x^\beta$.

harbors. A power-law fit to the data $(y = \alpha x^\beta)$ yielded a skill (r^2) of 0.83 and an exponent of 1.58 ± 0.41 (solid curve in Figure 13, panel i). The obtained power from the fitted function closely matches the exponent predicted by Equation 13, which suggests that $\hat{F}_h^V \propto (s_c^R)^{3/2}$. The findings on how the transport F_h^V depends on the tidal salinity range s_c^R explain the relatively weak contribution at HB-4 and HB-5, which are located in regions where s_c^R exhibits a local minimum (panel b in Figure 12).

4.3. Quantifying the Additional Salt Transport Induced by Tidal Trapping

We quantify the additional up-estuary directed salt transport resulting from tidal trapping and isolate the contributions of both advective out-of-phase exchange and diffusive processes (arising from the instantaneous vertically and laterally sheared salt flux), using Equation 5. For the diffusive contribution, we do not distinguish between vertically and laterally sheared salt flux but instead assess their combined effect, denoted as $\tilde{F}_S$. Moreover, we use the tidal varying part of F_h^A and $F_h^S = F_h^L + F_h^V$ (i.e., we subtracted the subtidal average) to ensure that our estimates are not influenced by subtidal salt transport into or out of the harbor basins.

Figure 14 shows the additional salt transport in the main channel resulting from channel-harbor exchange for HB-2 and HB-4 for a single tidal cycle. For both harbors, the additional up-estuary salt transport, $\tilde{F}_c^{\text{trp}}$, is predominantly due to $\tilde{F}_c^S$, which arises from vertically and laterally sheared exchange flows (see panels c and f in Figure 14). The additional salt transport varies over a distance approximately equal to the tidal excursion length, L_c, since this is the distance over which a redistribution of saltwater occurs due to tidal trapping (Dronkers, 1978; Dronkers & Van de Kreeke, 1986; Van Keulen et al., 2025). Within this range, the additional salt transport reaches a maximum near the down-estuary end of the tidal excursion relative to the position of the harbor. This downstream peak is explained by the asymmetry in F_h^S, which results in a more intense exchange near HW slack (shown in panels b and e in Figure 14).

To summarize the trapping effect over time, panels a and f in Figure 15 present the excursion-averaged additional salt transport over a spring–neap cycle for the different harbors, where the tidal excursion-averaged salt transport is defined as:

$$\overline{\tilde{F}_c^i} = \frac{1}{L_c}\int \tilde{F}_c^i dL_c, \tag{14}$$

where L_c is the tidal excursion length in the main channel, and the superscript ^{i} denotes the specific transport component. From Figure 15, it is clear that the additional salt transport resulting from tidal trapping is primarily due to $\overline{\tilde{F}_c^S}$, which is mainly driven by the vertically sheared salt flux resulting from density dynamics (see Section 4.2). The effect of out-of-phase exchange $\left(\overline{\tilde{F}_c^A} + \overline{\tilde{F}_c^C}\right)$, represented by the joint effect of the net down-estuary directed salt transport from the harbor $\left(\tilde{F}_c^A\right)$ and the compensating up-estuary salt transport $\left(\tilde{F}_c^C\right)$, is small and, for several harbors, even negative. This negative contribution has two causes. First, $\tilde{F}_c^A$ tends to become increasingly negative as the relative strength of diffusive channel–trap exchange increases. This is because the diffusive exchange causes the salinity in the harbor to rise as the basin begins to empty, making $\tilde{F}_c^A$ more negative compared to its value in the absence of diffusive exchange. Second, due to the import of low-salinity water from the OM channel (see Figure 5), the volume experiencing an up-estuary excursion has low salinity. This second effect is the primary source of the negative contribution to the advective out-of-phase exchange for harbors located near the junction (i.e., HB-1 to HB-4). Furthermore, the time series shows that the excursion-length-averaged additional salt transport exhibits little to no spring–neap variability at most locations. However, the influence of the diurnal tidal inequality is clearly present.

Panel g in Figure 15 shows the additional salt transport from tidal trapping, averaged over a spring-neap cycle, expressed relative to the tidally averaged salt transport associated with flushing by the river discharge in the main channel, $\frac{\overline{\tilde{F}_c^i}}{\overline{F_c^{\text{res}}}}$, also referred to as the diffusive salt fraction (Hansen & Rattray, 1966). This ratio quantifies the importance of tidal trapping to the overall up-estuary salt transport. It shows that the estimated contribution of tidal trapping in the individual harbors is 2%–10% of the up-estuary directed salt transport. Furthermore, the contributions of HB-4 and HB-5 are the weakest, despite being the largest harbors. This is a noteworthy results, as in expressions for tidal trapping in literature, tidal trapping generally increases with an increase in relative trap size. Their small contribution is further emphasized in panel h in Figure 15, which shows the diffusive salt fraction scaled by $\epsilon = \frac{\hat{Q}_c}{\hat{Q}_h}$. Their relatively small contribution is related to the limited contribution of $\overline{\tilde{F}_c^S}$. The two largest harbors (HB-4 and Hb-5) are located in a region where the tidal salinity range is small (Figure 12), which results in a small vertical shear related salt transport (see Section 4.2).

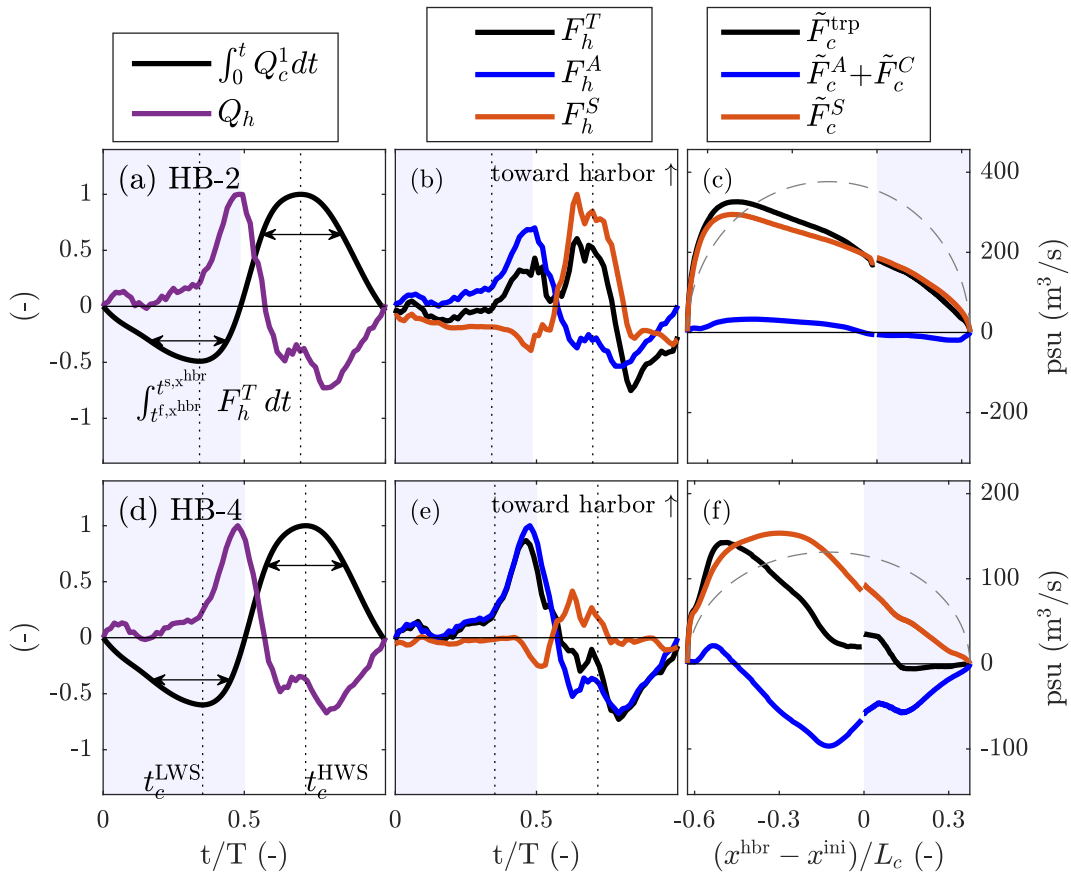

Figure 14. Illustration of the additional up-estuary salt flux $\tilde{F}_c^{\mathrm{trp}}$ quantified through Equation 5, shown for HB-2 and HB-4. (a), (d) Periods over which the integral in Equation 5 is evaluated. The double-headed arrows indicate the interval between the first and second moments when a plane moving along the main channel passes the harbor location (x^{har}). (b), (e) Instantaneous salt fluxes over the harbor entrance. (c), (f) The additional salt transport $\tilde{F}_c^{\mathrm{trp}}$, decomposed into contributions from advective out-of-phase exchange $(\tilde{F}_c^A + \tilde{F}_c^C)$ and from exchange that is diffusive in nature $(\tilde{F}_c^S)$. The gray dashed line shows the additional salt transport predicted by Equation B8, where s_c^R is attributed 7.5 and 2 psu, H_h is taken 15 and 14 m, and the ratio A_h/A_c is 0.5 and 0.6, for HB-2 and HB-4 (respectively). For all panels, blue shading indicates that the initial locations of parcels traveling with the cross-sectionally averaged discharge at $t = 0$ are situated up-estuary of x^{har}, whereas the white background indicates they are located down-estuary of x^{har}.

Overall, our analysis of the additional salt transport due to tidal trapping indicates that the relative contribution of harbors to salt dispersion is primarily determined by conditions in the main channel. Specifically, the salinity range s_c^R controls the strength of the exchange flow from vertically sheared salt flux between the channel and the harbors.

4.4. Relative Importance of Subtidal Exchange Compared to Tidal Trapping

Section 4.3 showed that larger harbors do not necessarily produce a greater additional salt transport through tidal trapping. This is due to the locally reduced diffusive channel–harbor exchange on intratidal time scales, which results from the local minimum in the tidal salinity range. In contrast, the net subtidal salt transport into or out of the harbors reflecting changes in salt storage related to spring–neap variability, river discharge change and storm surges, tends to increase with harbor size (Figure 16). This emphasizes that the influence of harbors can vary significantly depending on their size and their location within the system (i.e., in regions characterized by strong subtidal and/or intertidal salinity dynamics). In this context, the largest harbors act as sources or sinks of salt on a

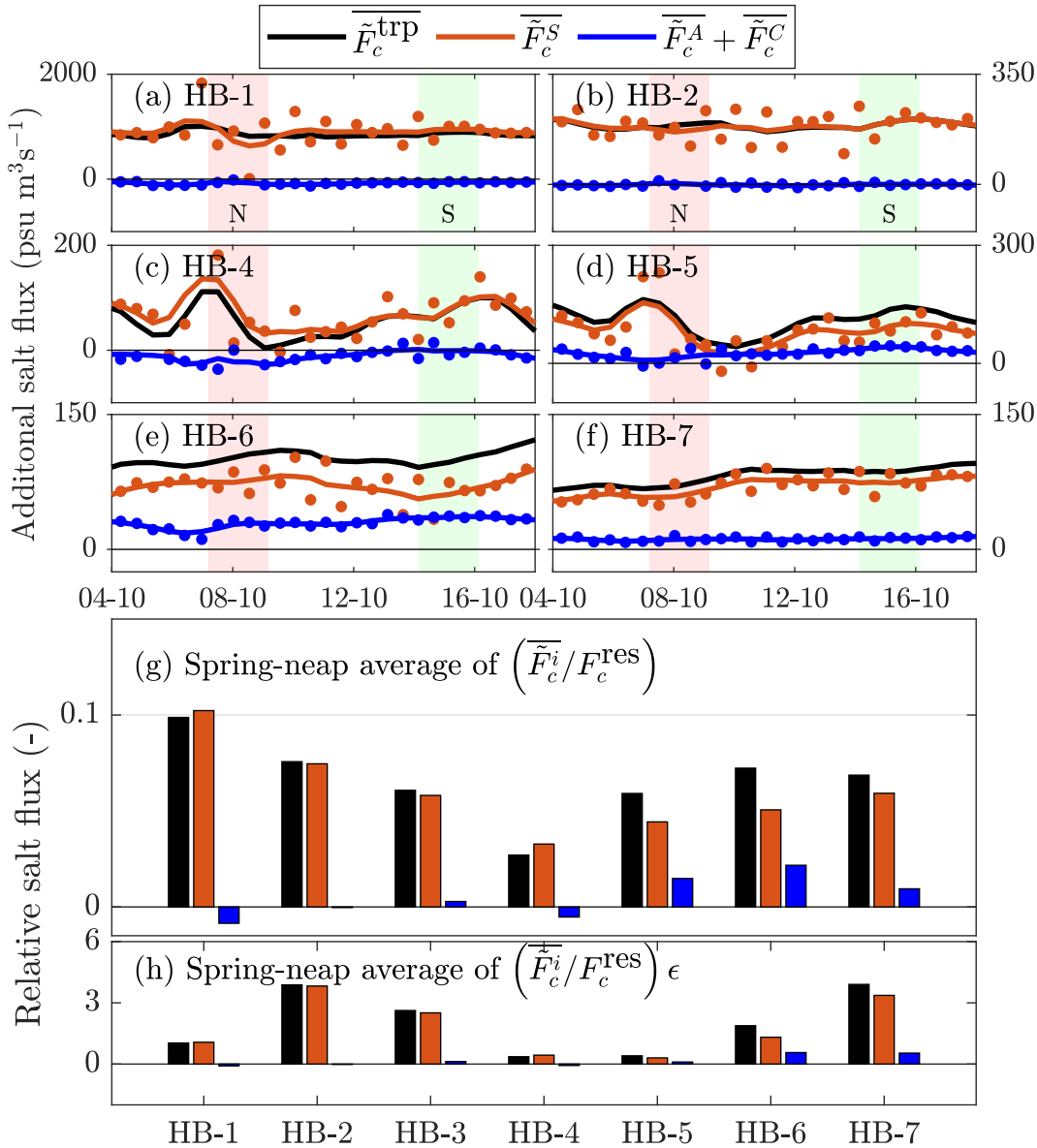

Figure 15. Overview of the additional (up-estuary) salt transport resulting from tidal trapping for the different harbors. (a–f) Tidal-excursion-averaged value of the additional salt transport resulting from tidal trapping, $\overline{\tilde{F}_c^{\mathrm{trp}}}$, and the individual contributions of advective out-of-phase exchange $\left(\overline{\tilde{F}_c^{A}} + \overline{\tilde{F}_c^{C}}\right)$ and diffusive exchange $\left(\overline{\tilde{F}_c^{S}}\right)$. Scatter points represent values obtained for individual tidal cycles, while the solid line indicates the smoothed response (running average over 5 tidal cycles). (g) The additional salt transport contributions $\left(\overline{\tilde{F}_c^{i}}\right)$, relative to F_c^{res} (i.e., expressed as a diffusive salt fraction), averaged over a spring–neap cycle. (h) Same as panel (g), but scaled by the relative discharge amplitude from the main channel to the harbor, $\epsilon = \hat{Q}_c/\hat{Q}_h$, to partially eliminate the influence of harbor size.

subtidal timescale, thereby contributing to the unsteadiness of the system and likely increasing its adjustment timescales. This notwithstanding, their contribution to the up-estuary salt transport through tidal trapping is minimal. Vice versa, in this particular case, the smaller basins contribute substantially to the additional salt transport via tidal trapping, but their role in salt storage on a subtidal timescale is limited.

5. Discussion

In this paper, we analyzed channel-harbor salt exchange and quantified the additional up-estuary salt transport resulting from tidal trapping in harbors along the partially stratified NM and New Waterway. The additional up-estuary salt transport resulting from tidal trapping is primarily caused by a vertically sheared channel–harbor

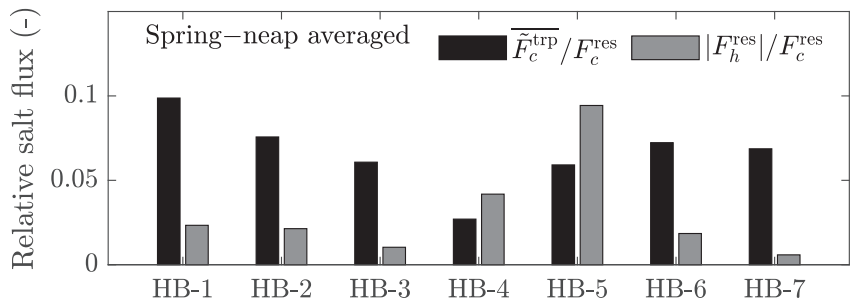

Figure 16. Comparison of the spring–neap averaged additional salt transport due to tidal trapping, $\overline{\tilde{F}_c^{\mathrm{trp}}}$, with the absolute subtidal salt transport into/out of the harbors, $|F_h^{\mathrm{res}}|$, both normalized by F_c^{res}. The comparison highlights the relative importance of channel–harbor exchange on intertidal versus subtidal time scales across the different harbors.

exchange flow driven by gravitational dynamics, while the contribution from tidal trapping through advective out-of-phase exchange is small. The conditions under which tidal trapping transitions from being dominated by advective out-of-phase exchange to being governed by diffusive processes from turbulence and density currents have been explored by Van Keulen et al. (2025). They evaluated the transition based on the tidal trapping Péclet number $P_{e,\mathrm{trapping}} = \left(\hat{U}_h \ell_h\right)/K_h$, where $\hat{U}_h$ is the velocity amplitude in the harbor, ℓ_h is the harbor or trap length, and K_h is a dispersion coefficient that parameterizes the instantaneous diffusive exchange. Van Keulen et al. (2025) found that for small tidal trapping Péclet numbers $\left(P_{e,\mathrm{trapping}} < 10^1\right)$, the contribution of advective out-of-phase exchange to the resulting up-estuary salt transport becomes negligible, and tidal trapping is then governed by diffusive exchange. From this, the dominance of diffusive exchange in relatively deep harbors can be readily understood. The current amplitude at the harbor entrance is inversely related to the depth of the harbor $\hat{U}_h \approx (2\hat{\eta}\ell_h)/(TH_h)$. Assuming that the diffusive exchange results from the vertically sheared salt transport driven by gravitational dynamics (see Section 4.2), the dispersion coefficient based on Equation 13 is expected to increase with harbor depth, following $K_h \propto H_h^{1/2}$. Using these relations, the tidal trapping Péclet number decreases rapidly with increasing basin depth, since $P_{e,\mathrm{trapping}} \propto H_h^{-3/2}$. Based on the observed vertically shear related fluxes at the HB-2 and HB-4, we estimated K_h to be 30 and 10 $\mathrm{m^2 s^{-1}}$ for the two harbors, using a dock length of $\ell_h = 2000$ m, with $\hat{U}_h = 0.02$ and 0.05 m/s. The resulting Péclet numbers are 1.33 and 10 for HB-2 and HB-4, respectively. These values indeed align with conditions where the additional salt transport mainly results from exchange that is diffusive in nature.

Tidal dispersion is often considered to be independent of the subtidal along-channel salinity gradient, in contrast to the parameterization of dispersion driven by the gravitational circulation (Hansen & Rattray, 1965; Monismith et al., 2002). Parameterizations of dispersion coefficients for tidal trapping driven by advective out-of-phase exchange (Dronkers, 1978; Schijf & Schönfled, 1953; Van Keulen et al., 2025) are independent of the salinity gradient, as demonstrated by Dronkers (1978). For tidal trapping driven by exchange that is diffusive in nature, Okubo (1973) derived an elegant expression, which, similar to the expression for advective out-of-phase exchange, is independent of the subtidal along-channel salinity gradient. In cases where tidal trapping results from a channel-harbor exchange driven by density dynamics, the resulting vertically sheared salt transport is found to be proportional to the tidal salinity range, according to: $\hat{F}_h^V \propto \left(s_c^R\right)^{3/2}$ (see Section 4.2). Under the assumption that s_c^R is solely the result of advection of a stationary salinity field, then $s_c^R \approx L_c \frac{\partial s_c^0}{\partial x}$. Assuming that the density-driven exchange in/out of the harbor varies sinusoidally in time and is in quadrature with the velocity in the main channel, a relation for the dispersion coefficients resulting from tidal trapping via channel-harbor exchange driven by density dynamics can be derived (see Appendix 2 for details):

$$K_c^{\mathrm{trp}}\left(x^{\mathrm{ini}}\right) = \frac{1}{8\pi}\sqrt{\frac{1}{2}}\left(\frac{B_h H_h}{A_c}\right)\left(\beta L \frac{\partial s_c^0}{\partial x} g H_h\right)^{1/2} L_c \cdot \left(1 - \left(2\frac{x^{\mathrm{ini}}}{L_c} - 1\right)^2\right)^{1/2}. \tag{15}$$

Equation 15 shows the dependence of dispersion on the ratio between harbor and channel cross-sectional area. The correct dimensions are determined by the propagation speed of the density current into the harbor $\sqrt{\beta L_c \frac{\partial s_c^0}{\partial x} g H_h}$ times the tidal excursion length in the main channel L_c, which provides an intuitive measure of the dispersive effect of tidal trapping driven by density dynamics. A noticeable difference with the formulations by Okubo (1973) and Dronkers (1978) is that Equation 15 depends on the salinity gradient according to $K_c^{\mathrm{trp}} \propto \sqrt{\frac{\partial s_c^0}{\partial x}}$. This difference can be explained from the fact that Okubo (1973) assumes an exchange-rate coefficient that represents the flux without specifying its driving processes. In contrast, for Equation 15, it is assumed that the channel-harbor exchange results from density dynamics, which introduces a dependence on the subtidal salinity gradient. Finally, although Equation 15 is derived under (highly) simplified conditions, it predicts our quantification of the additional salt transport reasonably well (see Figure 14).

The analysis of channel–harbor exchange reveals regions where the instantaneous vertically sheared salt flux exhibits a local minimum (Figure 13), which strongly reduces the net effect of tidal trapping (Figure 15). This minimum in the tidal salinity range s_c^R is not caused by the harbors themselves, but rather by differences in branch characteristics and sharp depth transitions within the NM. This is consistent with the overall limited role of harbor-induced tidal trapping, which contributes only about 5% of the up-estuary salt transport. The existence of this minimum in the tidal salinity range demonstrates that the contribution of harbors varies significantly between locations, depending on the nature of the exchange (as discussed above). However, to obtain a more complete understanding of the influence of harbors in a system like the Rhine–Meuse estuary, it is necessary to better resolve the interactions between individual branches and to determine how harbor effects combine or counteract one another. Moreover, the exchange between the main channel and side basins also affects main-channel dynamics, for instance through the formation of fronts (Bo & Ralston, 2020; Corlett & Geyer, 2020; Giddings et al., 2012). These processes can influence stratification and vertical mixing, while introducing additional shear that modifies dispersive mechanisms. To further advance understanding of trapping dynamics in side channels, it would be valuable to compare the additional salt transport resulting from the temporal storage studied herein with a decomposition of the tidal salt flux as derived by Dronkers and Van de Kreeke (1986) and more recently applied by Garcia and Geyer (2022) and Garcia et al. (2025). Such a comparison could help to relate the effect of trapping to shear-driven processes in the main channel. However, applying this type of analysis in a channel-network system remains challenging.

The main channel response to the additional salt transport from a trap differs between deep and shallow systems as follows. In a simplified 1D setting, an additional salt transport resulting from trapping will locally decrease the along-channel subtidal salinity gradient. This (local) reduction in the salinity gradient dampens the up-estuary salt transport driven by background dispersion. In deeper systems, the background dispersion is generally driven by the gravitation circulation, whereas in shallower systems, it is the result of tidal dispersion mechanisms. The dispersion coefficient for gravitational circulation has been derived as $K_G(x) \sim \frac{(\beta g)^2 H_c^8}{A_v^3}\left(\frac{\partial s_c^0}{\partial x}\right)^2$ (Hansen & Rattray, 1965; Monismith et al., 2002) and depends on the subtidal salinity gradient, whereas tidal dispersion is independent, or, as we discussed above, is weakly dependent on the subtidal salinity gradient. As a consequence, additional local dispersion will increase salinity levels up-estuary of the trap faster in well-mixed systems compared to systems where background dispersion is determined by the gravitation circulation. This is accompanied by a stronger decrease in the subtidal salinity gradient.

How harbors, or traps in general, influence the salt intrusion length depends on multiple aspects and is not easily estimated a priory. Exploratory model experiments were performed in which harbors were closed. The closure of HB-1, and the combined closure of HB-4 and HB-5 both resulted in a reduction of the salt intrusion length. In particular, the closure of HB-4 and HB-5 reduced up-estuary salinity levels. In contrast, the closure of HB-6 and HB-7 cause an increase in the salt intrusion length. Roelfzema and Van Os (1978) and Abraham et al. (1986) concluded that the harbor effect on salt intrusion in the Rhine-Meuse depends on two main counteracting mechanisms: additional mixing by temporal storage and release causing an increase, versus enhanced vertical mixing and an increase of the tidal prism causing a reduction. Scale models showed that closing harbors in the NM predominantly caused a reduction in the intrusion length. The latter agrees with our results for the HB-4 and HB-5, which contribute little to the additional salt-transport, but increase the tidal prism because of their size. Similar conclusions were drawn by Hendrickx and Pearson (2024), who explored the role of intertidal areas and found

that in partially stratified systems, intertidal areas reduce the estuarine circulation. Vice versa, in well-mixed systems, they found increasing salt intrusion. They did not quantify the relative contribution of individual mechanisms.

6. Conclusions

In this study, we investigate the exchange of salt between a partially stratified channel and its adjacent harbors, and examine how this exchange influences up-estuary salt transport along the NM within the Rhine-Meuse Estuary. During a field campaign, four shipboard surveys were conducted at two harbor basins. Analysis of the field observations indicates that the instantaneous salt exchange between the channel and a harbor is dominated by a vertically sheared, density-driven flow, which prevails over the contribution from barotropic filling and emptying of the harbors. The observed vertically sheared density-driven salt flux is less strong for the harbor where the tidal salinity range in the main channel was weaker, which limits the setup of the baroclinic pressure gradient driving this exchange flow. At one harbor, the observations revealed a current profile with a persistent mid-column outflow, which we attribute to a gradient in stratification driving a baroclinically induced acceleration that peaks in the core of the water column.

Numerical modeling results generalized the observations from the field, showing a marked reduction in the contribution of the vertically sheared salt flux for the harbors located in the region where the tidal salinity range is small. The salt transport by the vertically sheared exchange flow into and out of the harbor is empirically found to scale with the tidal salinity range to the $3/2$, which is in agreement with theory for density dynamics. Evaluation of the harbor-induced additional up-estuary salt transport (i.e., trapping-induced dispersion) showed that the additional salt transport is primarily induced by the channel-harbor salt flux component from the vertically sheared exchange flow. Due to the sensitivity of this exchange to the tidal salinity range, harbors located in regions with a smaller salinity range contributed significantly less to the net up-estuary salt transport. This explains the at first instance somewhat surprising observation that the largest harbors in the NM contributed the least to the up-estuary salt transport through tidal trapping.

Finally, we show that when channel–trap exchange is governed by density dynamics, the resulting tidal-trapping contribution to along-channel salt dispersion scales with the square root of the along-channel salinity gradient. This contrasts with classical parameterizations of advective out-of-phase exchange, which are independent of that gradient. This scaling follows from expressing tidal trapping as a dispersion coefficient under the assumption that the tidal salinity range arises from advection of the subtidal along estuary salinity profile.

Appendix A: The Salt Balance

A1. Decomposition of the Subtidal Salt Transport

The observed and modeled tidally averaged salt transport is decomposed to identify and quantify the underlying salt transport mechanisms. The following quantities are defined:

$$\begin{aligned} s(t,y,z) &= s^0 + s^1(t) + s^2(y,z) + s^3(t,y,z), \\ u(t,y,z) &= u^0 + u^1(t,z) + u^2(y,z) + u^3(t,y,z), \end{aligned} \tag{A1}$$

here the superscript ^{0} represents the cross-sectionally averaged and tidally averaged property, ^{1} is the cross-sectionally averaged but time-varying property, ^{2} is the cross-sectional variations of the time-averaged property (the steady shear component) and ^{3} is the time-varying cross-sectional variation (time-varying shear component). The subtidal salt transport is given by (Dronkers & Van de Kreeke, 1986; Garcia et al., 2022):

$$\begin{aligned} F &= F^{\text{res}} + F^{\text{tide}} + F^{\text{st,shear}} + F^{\text{var,shear}} \\ &= u^0 s^0 A^0 + \langle u^1 s^1 A \rangle + \int u^2 s^2 \, dA^0 + \langle \int u^3 s^3(t,y,z) \, dA \rangle, \end{aligned} \tag{A2}$$

where A^0 is the tidally averaged cross-sectional area, and the operator $\langle \cdot \rangle$ denotes a tidal average. The first term in Equation A2 is associated with flushing by the residual flow (F^{res}), which is primarily driven by the river

discharge. The second term, F^{tide} is the tidal oscillatory contribution, often referred to as the non-local salt flux contribution (Dronkers & Van de Kreeke, 1986). The third term, $F^{st,shear}$, captures the contribution of steady shear associated with the estuarine circulation (Lerczak et al., 2006; W. R. Geyer & MacCready, 2014), while the fourth term, $F^{var,shear}$, accounts for non-steady shear or local tidal salt transport (Garcia et al., 2022).

A2. Decomposition of the Measured Subtidal Salt Transport

Figure A1 presents the salt transport contributions computed from the 13-hr surveys and decomposed using Equation A2. During all four surveys, there was a substantial net seaward salt transport and the balance can be considered as unsteady (i.e., the tendency term in the salt balance is non-zero). The net seaward salt transport driven by F^{res} is consistently greater down-estuary of the harbor, with the difference balanced by a net salt transport from the harbor. Up-estuary salt transport occurred mostly through steady shear $\left(F^{st,shear}\right)$, with a greater contribution observed at the cross-section upstream of the harbor. The tidal oscillatory contribution $\left(F^{tide}\right)$ introduced a net seaward salt transport, except during the neap-tide survey at HB-4. Finally, the contribution of the non-steady shear $\left(F^{var,shear}\right)$ is small.

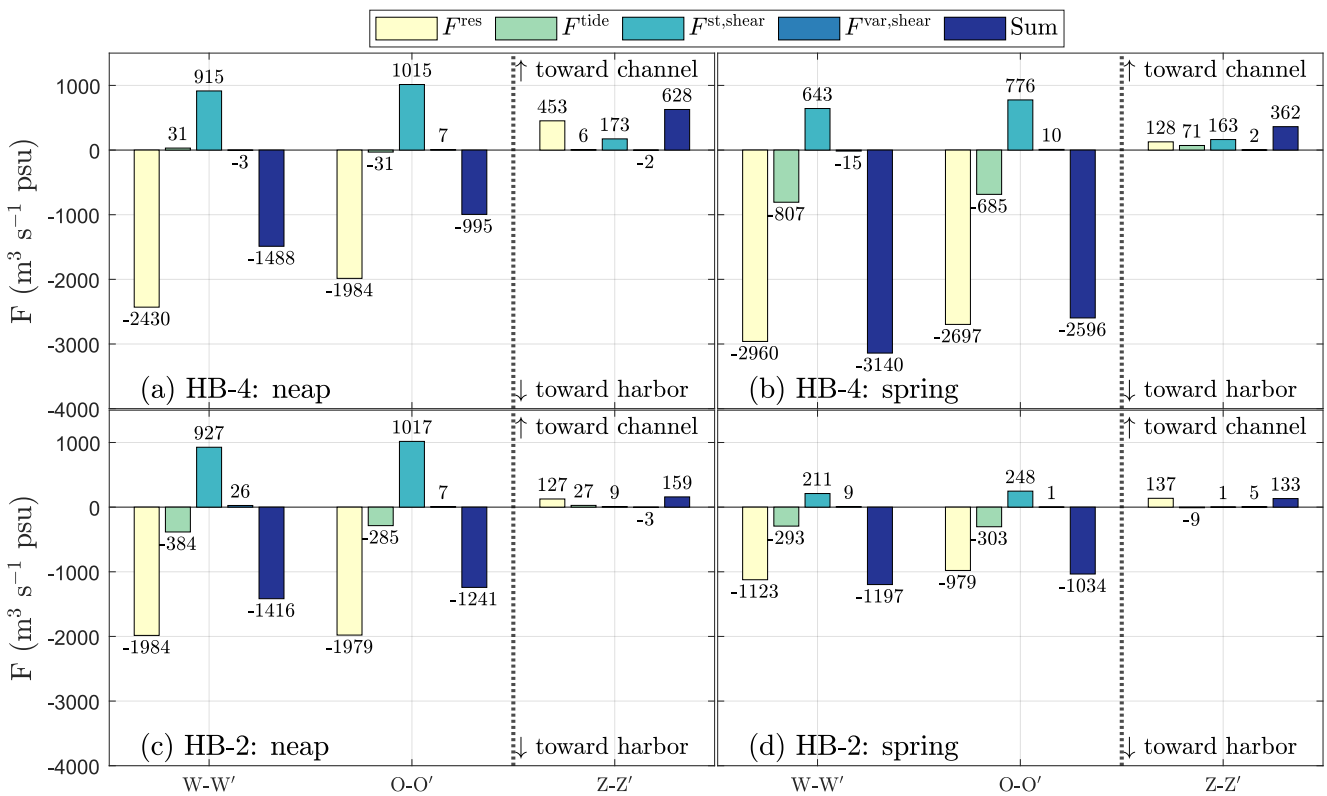

Figure A1. Salt transport decomposition of the tidally averaged salt transport (Equation A2) through the cross-sections surveyed during the 3-hr boat surveys. Results are shown for the two main channel cross-sections—down-estuary (W–W′) and up-estuary (O–O′) of the harbor—and for the cross-section at the harbor entrance (Z–Z′) (see Figures 1d and 1e). Panels show: (a) HB-4 neap tide, (b) HB-4 spring tide, (c) HB-2 neap tide, and (d) HB-2 spring tide. Numbers on the bars indicate the exact salt transport values. Positive values in the main channel correspond to up-estuary transport, whereas at the harbor entrance they indicate transport toward the channel. The subscripts $_c$ and $_h$, indicating whether a variable applies to the main channel or the harbor, have been omitted from the legend for clarity.

Appendix B: Expression for Tidal Trapping Driven by Gravitational Dynamics

To obtain an expression for tidal trapping in which the channel–trap exchange results from density dynamics, and where the salt transport associated with vertical shear reverses direction throughout the tidal cycle, we start from a simplified version of Equation 5. Assuming purely diffusive channel–trap exchange and a sinusoidal tidal current in the main channel, and setting $t = 0$ at LWS in the main channel, Equation 5 simplifies to:

$$\Delta F_c^{\mathrm{trp}}\left(x^{\mathrm{ini}}\right) = \int_{T/2-\Delta t_c}^{T/2+\Delta t_c} F_h^V, dt, \tag{B1}$$

where the integral bounds are relative to HWS, and Δt_c is the time window bounded by the moments for which the plane passes the along-channel position of the trap for the first and second time. Based on Equation 13, we assume that the amplitude of the diffusive transport is proportional to the salt transport expected from density dynamics (Benjamin, 1968), with the density difference is approximated as $\Delta\rho = \rho_0 \beta s_c^R$, that is, equal to the salinity range (van Maren et al., 2009):

$$\hat{F}_h^V \approx \frac{1}{4}(\beta g)^{1/2}\left(s_c^R H_h\right)^{3/2} B_h. \tag{B2}$$

Alternatively, it may be assumed that the maximum salinity difference between the back of the harbor and the channel is given by $\Delta\rho = \frac{1}{2}\rho_0 \beta s_c^R$. This corresponds to the situation where the salinity at the back of the basin remains equal to the tidally averaged salinity in the main channel. Then, we obtain:

$$\hat{F}_h^V \approx \frac{1}{8}\sqrt{\frac{1}{2}}(\beta g)^{1/2}\left(s_c^R H_h\right)^{3/2} B_h. \tag{B3}$$

When s_c^R is the result of advection of an arrested salinity field, we can define $s_c^R = L_c \frac{\partial s_c^0}{\partial x}$ where L_c is the tidal excursion length in the main channel. Equations B2 and B3 provide an estimate of the magnitude of the exchange between channel and trap. Assuming that F_h^V varies sinusoidally and peaks at slack water —i.e., it is in quadrature with the cross-sectionally averaged current— we define:

$$F_h^V \approx \hat{F}_h^V \cos(\omega t). \tag{B4}$$

It should be noted that Equation B4 gives an overly simplified representation and ideally would be replaced by a more theoretically substantiated formulation. Substituting Equation B4 into Equation B1, evaluation of the integral results in:

$$\Delta F_c^{\mathrm{trp}}\left(x^{\mathrm{ini}}\right) = \frac{2}{w}\hat{F}_h^V \sin(w\Delta t_c). \tag{B5}$$

To simplify Equation B5, the time window Δt_c can be expressed in terms of the initial position x^{ini} of the plane that moves with the tidally varying discharge component at $t = 0$, using that the distance traveled by this plane is expressed as $\Delta x = \frac{1}{2}L_c(1 - \cos(\omega t))$:

$$\Delta t_c = \frac{T}{2} - \frac{1}{\omega}\cos^{-1}\left(\frac{2x^{\mathrm{ini}}}{L_c} - 1\right). \tag{B6}$$

Substituting this into Equation B5 results in the following expression:

$$\Delta F_c^{\mathrm{trp}}\left(x^{\mathrm{ini}}\right) = \frac{2}{w}\hat{F}_c^V \cdot \left[1 - \left(\frac{2x^{\mathrm{ini}}}{L_c} - 1\right)^2\right]^{1/2}. \tag{B7}$$

Equation B1 represents the total transport over a tidal cycle. Expressing F_c^{trp} as the tidally averaged additional salt transport and substitution of Equation B2 results in:

$$F_c^{\text{trp}}\left(x^{\text{ini}}\right) = \frac{1}{4\pi} B_h (\beta g)^{1/2} \left(s_c^R H_h\right)^{3/2} \cdot \left[1 - \left(\frac{2x^{\text{ini}}}{L_c} - 1\right)^2\right]^{1/2}. \tag{B8}$$

Alternatively, Equation B3 can be substituted, which yields:

$$F_c^{\text{trp}}\left(x^{\text{ini}}\right) = \frac{1}{8\pi}\sqrt{\frac{1}{2}} B_h (\beta g)^{1/2} \left(s_c^R H_h\right)^{3/2} \cdot \left[1 - \left(\frac{2x^{\text{ini}}}{L_c} - 1\right)^2\right]^{1/2}. \tag{B9}$$

Given that the system is in steady-state and there is no net salt transport through the cross-sections, $K_c^{\text{trp}} = F_c^{\text{trp}} / \left(A_c^0 \frac{\partial s_c^0}{\partial x}\right)$, which results in the following expression when we use $s_c^R = L_c \frac{\partial s_c^0}{\partial x}$ in Equation B8:

$$K_c^{\text{trp}}\left(x^{\text{ini}}\right) = \frac{1}{4\pi}\left(\frac{H_h B_h}{A_c}\right)\left(\beta L_c \frac{\partial s_c^0}{\partial x}\right)^{1/2} (g H_h)^{1/2} L_c \cdot \left[1 - \left(\frac{2x^{\text{ini}}}{L_c} - 1\right)^2\right]^{1/2}, \tag{B10}$$

or, when we use $s_c^R = L_c \frac{\partial s_c^0}{\partial x}$ in Equation B9:

$$K_c^{\text{trp}}\left(x^{\text{ini}}\right) = \frac{1}{8\pi}\sqrt{\frac{1}{2}}\left(\frac{H_h B_h}{A_c}\right)\left(\beta L \frac{\partial s_c^0}{\partial x}\right)^{1/2} (g H_h)^{1/2} L_c \cdot \left[1 - \left(\frac{2x^{\text{ini}}}{L_c} - 1\right)^2\right]^{1/2}. \tag{B11}$$

Conflict of Interest

The authors declare no conflicts of interest relevant to this study.

Availability Statement

The data supporting this study are available at https://doi.org/10.5281/zenodo.16406724. The water-level data from the Rhine–Meuse estuaries used in this study are publicly available at https://waterinfo.rws.nl.

Acknowledgments
This project is part of the SALTISolutions Perspective Programme and is funded by Dutch Research Council NWO, Rijkswaterstaat, Deltares, Port of Rotterdam, Hydrologic, Hoogheemraadschap van Schieland De Krimpenerwaard, Hoogheemraadshap Rijnland and Royal BAM. We would like to thank Rijkswaterstaat and the Port of Rotterdam for their support in the data collection.

References

Abraham, G., de Jong, P., & Van Kruiningen, F. (1986). Large-scale mixing processes in a partly mixed Estuary. *Physics of Shallow Estuaries and Bays*, *16*, 5–21.

Armi, L., & Farmer, D. M. (1986). Maximal two-layer exchange through a contraction with barotropic net flow. *Journal of Fluid Mechanics*, *164*, 27–51. https://doi.org/10.1017/s0022112086002458

Benjamin, T. B. (1968). Gravity currents and related phenomena. *Journal of Fluid Mechanics*, *31*(2), 209–248. https://doi.org/10.1017/s0022112068000133

Biemond, B., Kranenburg, W. M., Huismans, Y., de Swart, H. E., & Dijkstra, H. A. (2025). Dynamics of salt intrusion in complex estuarine networks: An idealised model applied to the rhine–meuse Delta. *Ocean Science*, *21*(1), 261–281. https://doi.org/10.5194/os-21-261-2025

Bo, T., & Ralston, D. K. (2020). Flow separation and increased drag coefficient in estuarine channels with curvature. *Journal of Geophysical Research: Oceans*, *125*(10), e2020JC016267. https://doi.org/10.1029/2020jc016267

Chatwin, P. (1976). Some remarks on the maintenance of the salinity distribution in estuaries. *Estuarine and Coastal Marine Science*, *4*(5), 555–566. https://doi.org/10.1016/0302-3524(76)90030-x

Corlett, W. B., & Geyer, W. R. (2020). Frontogenesis at estuarine junctions. *Estuaries and Coasts*, *43*(4), 722–738. https://doi.org/10.1007/s12237-020-00697-1

Cox, J. R., Huismans, Y., Knaake, S., Leuven, J., Vellinga, N., Van der Vegt, M., et al. (2021). Anthropogenic effects on the contemporary sediment budget of the lower rhine-meuse Delta channel network. *Earth's Future*, *9*(7), e2020EF001869. https://doi.org/10.1029/2020ef001869

Deltares. (2021) In *Delft3d-flow user manual (version 3.15 ed.)* [Computer software manual]. Software manual. https://content.oss.deltares.nl/delft3d4/Delft3D-FLOW_User_Manual.pdf

De Nijs, M. A., Winterwerp, J. C., & Pietrzak, J. D. (2009). On harbour siltation in the fresh-salt water mixing region. *Continental Shelf Research*, *29*(1), 175–193. https://doi.org/10.1016/j.csr.2008.01.019

Dijkstra, Y. M., & Schuttelaars, H. M. (2021). A unifying approach to subtidal salt intrusion modeling in tidal estuaries. *Journal of Physical Oceanography*, *51*(1), 147–167. https://doi.org/10.1175/jpo-d-20-0006.1

Dijkstra, Y. M., Schuttelaars, H. M., & Kranenburg, W. M. (2022). Salt transport regimes caused by tidal and subtidal processes in narrow estuaries. *Journal of Geophysical Research: Oceans*, *127*(12), e2021JC018391. https://doi.org/10.1029/2021jc018391

Dronkers, J. (1978). Longitudinal dispersion in shallow well-mixed estuaries. *Coastal engineering*, *1978*, 2761–2777.
Dronkers, J., & Van de Kreeke, J. (1986). Experimental determination of salt intrusion mechanisms in the volkerak Estuary. *Netherlands Journal of Sea Research*, *20*(1), 1–19. https://doi.org/10.1016/0077-7579(86)90056-6
Eysink, W. (1989). Sedimentation in harbour basins. Small density differences May cause serious effects. In *International harbour congress*.9th.
Fischer, H. B., List, J. E., Koh, C. R., Imberger, J., & Brooks, N. H. (1979). *Mixing in inland and coastal waters*. Academic Press.
Friedrichs, C. T. (2010). Barotropic tides in channelized estuaries. *Contemporary issues in estuarine physics*, *27*, 61.
Garcia, A. M. P., Bo, T., Geyer, W. R., & Ralston, D. K. (2025). Topographically induced dispersion in a salt marsh Estuary. *Journal of Physical Oceanography*.
Garcia, A. M. P., & Geyer, W. R. (2022). Tidal dispersion in short estuaries. *Journal of Geophysical Research: Oceans*, *128*(2), e2022JC018883. https://doi.org/10.1029/2022jc018883
Garcia, A. M. P., Geyer, W. R., & Randall, N. (2022). Exchange flows in tributary creeks enhance dispersion by tidal trapping. *Estuaries and Coasts*, *45*(2), 363–381. https://doi.org/10.1007/s12237-021-00969-4
Geyer, W., Ralston, D., Haller, M., Bassett, C., & Honegger, D. (2024). The structure and dynamics of an estuarine tidal intrusion front. *Journal of Geophysical Research: Oceans*, *129*(2), e2023JC020371. https://doi.org/10.1029/2023jc020371
Geyer, W. R., & MacCready, P. (2014). The estuarine circulation. *Annual Review of Fluid Mechanics*, *46*, 175–197.
Geyer, W. R., & Ralston, D. K. (2015). Estuarine frontogenesis. *Journal of Physical Oceanography*, *45*(2), 546–561. https://doi.org/10.1175/jpo-d-14-0082.1
Geyer, W. R., & Signell, R. P. (1992). A reassessment of the role of tidal dispersion in estuaries and bays. *Estuaries*, *15*(2), 97–108. https://doi.org/10.2307/1352684
Giddings, S. N., Fong, D. A., Monismith, S. G., Chickadel, C. C., Edwards, K. A., Plant, W. J., et al. (2012). Frontogenesis and frontal progression of a trapping-generated estuarine convergence front and its influence on mixing and stratification. *Estuaries and Coasts*, *35*(2), 665–681. https://doi.org/10.1007/s12237-011-9453-z
Hansen, D. V., & Rattray, M. (1965). Gravitational circulation in straits and estuaries. *Journal of Marine Research*, *23*, 104–122.
Hansen, D. V., & Rattray, M. J. (1966). New dimensions in Estuary classification. *Limnology & Oceanography*, *11*(3), 319–325. https://doi.org/10.4319/lo.1966.11.3.0319
Hendrickx, G. G., & Pearson, S. G. (2024). On the effects of intertidal area on estuarine salt intrusion. *Journal of Geophysical Research: Oceans*, *129*(9), e2023JC020750. https://doi.org/10.1029/2023jc020750
Jongbloed, H., Vermeulen, B., & Hoitink, A. J. F. (2025). Physics-informed estimation of tidal and subtidal flow fields from ADCP repeat transect data. *Water Resources Research*, *61*(1), e2023WR036038.
Kranenburg, C. (1996). *Density currents. Reader lecture b81*. Delft Technical University. (in Dutch).
Kranenburg, W., Van der Kaaij, T., Tiessen, M., Friocourt, Y., & Blaas, M. (2022). Salt intrusion in the rhine meuse delta: Estuarine circulation, tidal dispersion or surge effect. In *Proceedings of the 39th iahr world congress* (pp. 19–24).
Lerczak, J. A., Geyer, W. R., & Chant, R. J. (2006). Mechanisms driving the time-dependent salt flux in a partially stratified estuary. *Journal of Physical Oceanography*, *36*(12), 2296–2311. https://doi.org/10.1175/jpo2959.1
Leuven, J. R., Niesten, I., Huismans, Y., Cox, J. R., Hulsen, L., Van der Kaaij, T., & Hoitink, A. (2023). Peak water levels rise less than mean sea level in tidal channels subject to depth convergence by deepening. *Journal of Geophysical Research: Oceans*, *128*(4), e2022JC019578. https://doi.org/10.1029/2022jc019578
Monismith, S. G., Kimmerer, W., Burau, J. R., & Stacey, M. T. (2002). Structure and flow-induced variability of the subtidal salinity field in northern San Francisco Bay. *Journal of Physical Oceanography*, *32*(11), 3003–3019. https://doi.org/10.1175/1520-0485(2002)032<3003:safivo>2.0.co;2
Niesten, I., Huismans, Y., & Hoitink, A. (2024). Ebb-dominant mixing increases the seaward sediment flux in a stratified Estuary. *Journal of Geophysical Research: Oceans*, *129*(12), e2024JC021201. https://doi.org/10.1029/2024jc021201
Nunes, R., & Simpson, J. (1985). Axial convergence in a well-mixed Estuary. *Estuarine, Coastal and Shelf Science*, *20*(5), 637–649. https://doi.org/10.1016/0272-7714(85)90112-x
Okubo, A. (1973). Effect of shoreline irregularities on streamwise dispersion in estuaries and other embayments. *Netherlands Journal of Sea Research*, *6*(1–2), 213–224. https://doi.org/10.1016/0077-7579(73)90014-8
Ralston, D. K., & Stacey, M. T. (2005). Longitudinal dispersion and lateral circulation in the intertidal zone. *Journal of Geophysical Research*, *110*(C7), C07015. https://doi.org/10.1029/2005jc002888
Roelfzema, A., & Van Os, A. (1978). Effect of harbours on salt intrusion in estuaries. *Coastal engineering*, *1978*, 2810–2826.
Schijf, J., & Schönfled, J. (1953). Theoretical considerations on the motion of salt and fresh water.
Simpson, J. H., Brown, J., Matthews, J., & Allen, G. (1990). Tidal straining, density currents, and stirring in the control of estuarine stratification. *Estuaries*, *13*(2), 125–132. https://doi.org/10.2307/1351581
Van Keulen, D., Kranenburg, W. M., & Hoitink, A. J. (2025). Tidal trapping and its effect on salinity dispersion in well-mixed estuaries revisited. *Estuaries and Coasts*, *48*(6), 153. https://doi.org/10.1007/s12237-025-01579-0
van Maren, D. S., Winterwerp, J. C., Sas, M., & Vanlede, J. (2009). The effect of dock length on harbour siltation. *Continental Shelf Research*, *29*(11–12), 1410–1425. https://doi.org/10.1016/j.csr.2009.03.003
Vermeulen, B., Sassi, M., & Hoitink, A. (2014). Improved flow velocity estimates from moving-boat adcp measurements. *Water Resources Research*, *50*(5), 4186–4196. https://doi.org/10.1002/2013wr015152
Warner, J., Schoellhamer, D., Burau, J., & Schladow, G. (2002). Effects of tidal current phase at the junction of two straits. *Continental Shelf Research*, *22*(11–13), 1629–1642. https://doi.org/10.1016/s0278-4343(02)00026-2